Three-scale bridging for woven composites using homogenization techniques

Kevin Spilker[a], Van-Dung Nguyen[a,1], Ling Wu[a], Ludovic Noels[a,*]

[a]*Computational & Multiscale Mechanics of Materials, University of Liège, Belgium*

Preprint submitted to European Journal of Mechanics - A/Solids. (C) 2023; Licensed under the Creative Commons (CC-BY-NC-ND); formal publication on: 10.1016/j.euromechsol.2023.104974

Abstract

Woven composites have a multiscale character, whose structural response is affected by mechanisms on different lower scales. The predicted macroscopic response of a carbon fiber reinforced woven composite is achieved by model order reduction and homogenization techniques, taking into account the structures and mechanisms on both mesoscopic and microscopic scales. Reduced order models based on piecewise uniform fields and mean field homogenization are integrated for the micro-meso-macro upscaling to finally determine the effective macroscopic response of a woven unit cell. A spatial decomposition for the woven composite unit cell on the mesoscale is implemented, achieving the model order reduction by taking into account the local microstructure of the yarns as well as inelastic fields emerging under selected deformation conditions. Following, different numerical tests are performed on the woven unit cell, containing complex and inelastic loading histories. Macroscopic homogenized predictions following the reduced order models and full-field direct numerical simulations are compared. Very high accuracies are achieved by the employed reduced order models, allowing for great computational savings.

Keywords: Textile composites, Anisotropic materials, Multiscale analysis, Reduced order model, Clustering

1. Introduction

The typical scale of interest in the computational mechanics of composite materials, is the structural, or macroscopic, scale. Due to the complexity of non-linear composite structures on their meso and microscales, no direct constitutive relations for the macroscopic material behavior are available. With the lack of accurate macroscopic constitutive relations,

*Corresponding author

Email addresses: Kevin.Spilker@uliege.be (Kevin Spilker), VanDung.Nguyen@uliege.be (Van-Dung Nguyen), l.wu@ulg.ac.be (Ling Wu), l.noels@ulg.ac.be (Ludovic Noels)

[1]Postdoctoral Researcher at the Belgian National Fund for Scientific Research (FNRS)

the precise analysis of the macroscopic mechanical behavior requires the consideration of mechanisms on the lower scales, where constitutive relations of the individual composite constituents are often available.

Computational analyses linking the materials behavior on the macroscopic scale to the mechanisms on the heterogeneous meso- or microscale, are known as multiscale simulations and typically rely on a principle that is known as the mechanical homogenization (Kanouté et al., 2009; Charalambakis, 2010; Geers et al., 2010; Saeb et al., 2016; Geers et al., 2017; Yvonnet, 2019, e.g.). In homogenization-based multiscale methods, the deformation state at one point of the macroscopic domain constitutes a new boundary value problem (BVP) applied on a mesoscopic or microscopic domain, assumed to contain all structural features and called representative volume element (RVE).

Analytical and semi-analytical approaches for the mechanical homogenization of composite materials exist: While the analytically homogenized macroscopic behavior is derived from certain upper and lower bounds (Voigt, 1889; Reuss, 1929; Hashin and Shtrikman, 1962, 1963; Talbot and Willis, 1985), semi-analytical mean field homogenization (MFH) approaches rely on estimated interaction functions between the single constituting material phases of the composite, with assumed per-phase uniform fields. The variational approach pioneered by Ponte Castañeda (1991) builds the foundation for many subsequent homogenization schemes by introducing a linear comparison composite (LCC) with linear properties being equivalent to the linearized effective properties of the actual non-linear composite. Recent MFH approaches for predictions of the non-linear responses of composite materials, are formulated on the basis of the LCC (Doghri et al., 2011; Wu et al., 2013a, 2017). MFH approaches have the ability to deliver homogenized composite estimations, in particular for composites with fully random structues, with very low computational requirements. The compromise of MFH is the inability to provide reliable predictions for complex composite structures, as woven composites in particular.

Increasing computational capabilities nowadays allow the use of direct numerical simulations (DNS), and therefore an accurate consideration of the micromechanics, for the mechanical homogenization, as FE^2 (Feyel, 1999; Kouznetsova et al., 2001, e.g.) or Fast Fourier transformation (FFT) based approaches (Moulinec and Suquet, 1994, 1998). However, complex heterogeneous microstructures can require extremely fine discretizations, implying the requirement of immense computational power or time for the macroscopic numerical solution.

Remedy for the issue of extreme computational efforts, and nonetheless the capability to accomplish accurate predictions for composite materials with complex microstructures, is achieved by surrogate models with a computationally much lighter solution stages. These surrogate models can be either so-called reduced order models (ROMs) achieved by mathematical model order reduction (MOR) techniques, data-driven models making use of machine learning methods like deep material networks, or approximations of underlying analytical micromechanical algorithms, providing a scale-coupling between global and local fields. These analytical micromechanical formulations are built by particular influence functions, quantifying interactions due to local fields, and spatial convolution theorems. Using the micromechanical algorithms as light surrogate models, they are used in combination

with spatial subdivision techniques into subdomains and approximated by the assumption of piecewise uniform, or average, fields (Dvorak, 1990) and effective interaction operators between the subdomains. Practically, the decomposition of a material domain into subdomains may be achieved by means of statistical divisions, so-called clustering techniques. For physically sensible decompositions of the microstructural domain, the clustering algorithm can be fed by several micromechanical fields under specific boundary conditions, gathered through full-field DNS of the composite structure in the offline stage (Liu et al., 2016; Wulfinghoff et al., 2018; Spilker et al., 2022). The consideration of piecewise uniform fields has similarities to MFH approaches. However, the spatial decompositions and the estimation of interaction functions in the actual composite structure through DNS in the so-called offline stage, allow to circumvent microstructural preassumptions. With the achieved reduction of both the integration domain and the degrees of freedom, the spatial division will be referred to as the MOR step and the methods relying on piecewise uniform fields as ROMs.

The pioneering approach for the piecewise uniform field homogenization is the transformation field analysis (TFA) by Dvorak (1992). The analytical TFA algorithm is based on the definition of the separation of elastic and inelastic fields (referred to as eigenfields) and elastic eigenstrain interaction functions inside the heterogeneous medium. The TFA leads to traditionally overstiff modeled inelastic responses of the composite material when reasonable numbers of subdomains are used, explained with a loss of physics due to piecewise uniform approximations of spatially heterogeneous inelastic fields and consequently underestimated interaction effects. Spilker et al. (2022) extended the spatial decomposition from the consideration of purely elastic deformation fields towards the integration of dominant inelastic fields under typical deformation conditions of the particular composite structure, and achieved improved convergence of the TFA predictions towards DNS results under increasing numbers of subdomains. The reason for improved inelastic approximations of the composite are improved captures of the inelastic field interactions through the enhanced spatial decomposition. No increasing prediction errors were encountered when the stiffness contrast between the phases or the structural anisotropy increases. Furthermore was shown that very accurate results are achieved for composite systems consisting of an inelastic inclusion phase in an inelastic matrix. Using clustering techniques, too high amounts of inelastic field information may lead to diffuse subdomain identifications or the requirement of unreasonably large numbers of subdomains. Therefore, in order to guarantee accurate coverage of the computed inelastic fields by the subdomains without too large number of degrees of freedom, the number of possibly considered deformation modes in the offline stage is limited. With a spatial decomposition that bases on a limited number of deformation modes, even when representing the most typical deformation modes, a loss of the physics of the inelastic problem may still occur under arbitrary inelastic deformation conditions or extended loading histories, leading to inelastic fields that strongly deviate from the ones encountered in the offline stage. A recent strategy for the improved account for localized effects during inelastic loading histories was provided by Ferreira et al. (2022), proposing an adaptive re-clustering procedure during the solution stage. The TFA, even when relying on an inelasticity based spatial decomposition, may still lead to too stiff inelastic predictions of composites that consist of elevated volume fractions of elastic inclusions inside an inelas-

tic matrix phase due to underestimated eigenstrain interactions (Spilker et al., 2022). For better estimates of the composites behavior, Chaboche et al. (2001) developed a correction for the eigenstrains based on a consideration of the asymptotic tangent strain concentration tensors of the subdomains. Building on the piecewise uniform approximation of the local fields, several approaches explicitly take into account the local microscopic inelastic fields. Fish et al. (1997) considered a serial expansion of stresses and eigenstrains based on the contributions on the different scales. In the non-uniform TFA (NTFA) by Michel and Suquet (2003), localized inelastic mechanisms are accounted for by the integration of fully non-uniform eigenstrain fields, composed by a finite set of a-priori determined inelastic strain modes. Michel and Suquet (2016) have applied a tangent second-order (TSO) expansion of the dissipation potential, which corresponds to a reduction of the evolution equations related to the reduced internal variables. Alternatively, the NTFA was extended by Fritzen and Leuschner (2013) towards a potential-based formulation (pRBMOR), where the evolution laws for the internal variables are derived from variational principles. The pRBMOR allows for the modeling of any kind of material behavior controlled by a dissipation potential, referred to as Generalized Standard Material (GSM) classes.

Alternative descriptions of the micromechanics in heterogeneous composite media, as, e.g., Kröner (1977, 1978), make use of the Lippmann-Schwinger equation (Lippmann and Schwinger, 1950), relying on a homogeneous reference medium and interactions due to local polarization stress fields (Eshelby, 1957; Hashin and Shtrikman, 1962, 1963). The interactions are expressed through the Green's influence function of the homogeneous reference medium. The first piecewise uniform field ROM approach based on the Lippmann-Schwinger equation is the self-consistent clustering analysis (SCCA) by Liu et al. (2016, 2018). In the SCCA approach, the homogeneous reference medium is assumed to be isotropic. The isotropic stiffness operator represents the isotropized homogenized response of the composite and can be adapted during nonlinear responses by computing the instantaneous homogenized Lamé parameters. The Green's interaction tensors, in the SCCA algorithm computed analytically, are updated during the solution stage accordingly to the updated stiffness of the reference medium. An approach similar to the SCCA is the Hashin-Shtrikman (HS) type analysis (Wulfinghoff et al., 2018; Cavaliere et al., 2020), relying on an isotropic secant stiffness operator. In this method, elastic influence functions are determined numerically by pre-simulations. With an assumed constant Poisson ratio of the reference medium, the stiffness tensor and the Green's interaction tensors of the reference medium can be easily adapted during nonlinearities purely by scaling with the updated secant shear modulus of the composite. Originally implemented for the modeling of nonlinear elastic materials behavior without the evolution of internal state variables, the HS type analysis was later applied to elasto-plastic materials by Castrogiovanni et al. (2021). The validity of the TFA and the HS type homogenization techniques for the responses of various composite material systems was evaluated in detail by Spilker (2022).

This work focuses on the clustering based ROM of woven composite structures. The mesoscale woven composite unit cell consists of yarns, spanning the so-called ply-plane, surrounded by a pure matrix material phase. The yarns are composite materials themselves, consisting of long fibers embedded in the same matrix material. Consequently, a woven

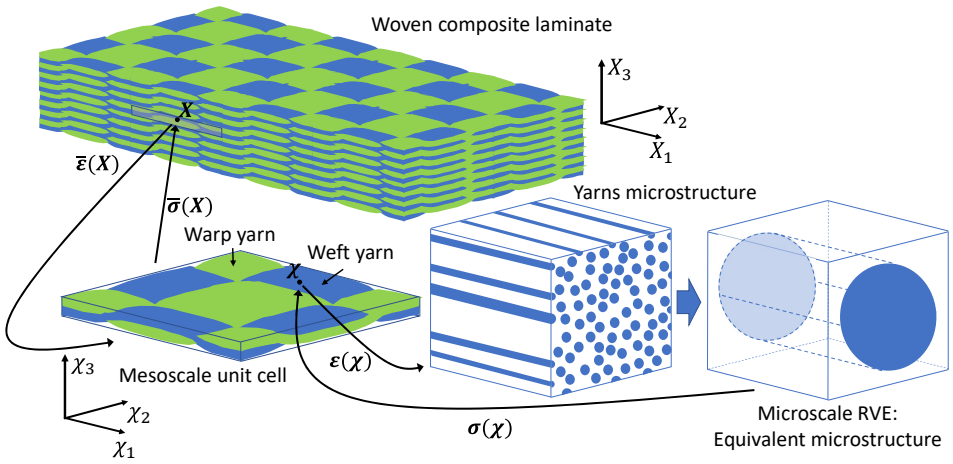

Figure 1: Schematic demonstration of a mechanical full-field problem of a woven structure considering the associated scales. The deformation state $\overline{\boldsymbol{\varepsilon}}(\boldsymbol{X})$ at a certain macroscopic material point $\boldsymbol{X}$ inside a structural woven composite states the boundary problem for the unit cell, representing the woven mesostructure. The mesoscopic material points $\boldsymbol{\chi}$ of the yarns in the mesoscale unit cell are locally represented by a UD fibrous microstructure. Following from the mesoscopic deformation state $\boldsymbol{\varepsilon}(\boldsymbol{\chi})$ at the material points $\boldsymbol{\chi}$ in the yarns, the MFH is used for the computation of the homogenized response $\boldsymbol{\sigma}(\boldsymbol{\chi})$ of the equivalent microstructural RVE, where the fibrous phase is represented by one inclusion/fiber in the matrix phase (Section 2.2.1). The macroscopic stress response of the woven unit cell $\overline{\boldsymbol{\sigma}}(\boldsymbol{X})$ follows from the consideration of the complete local field $\boldsymbol{\chi}$.

composite can be classified as a three-scale material, where the evaluation of the structural behavior is affected by mechanisms on the mesoscopic and microscopic scales (Fig. 1). The non-uniform microstructural configuration of the yarns due to locally varying yarn orientations needs to be respected by the spatial division into subdomains, in order to gather only material points with similar responses in the same subdomain and guarantee valid predictions of the unit cell using piecewise uniform approximations. For this sake, an adapted clustering of the mesoscale material domain was implemented, taking into account the non-uniform microstructure of the yarns. In the work by Han et al. (2020), the macroscopic response of the unit cell was modeled by the SCCA scale coupling, with mesoscopic deformation fields approximated by piecewise uniform fields. Since the heterogeneous character of the yarns microstructure was not explicitly respected during the solution stage, homogenized elastic properties of the yarns were determined offline by microscale DNS, and the nonlinear behavior of the woven unit cell was modeled based on the a-priori evaluation of a yield criterion for the particular unit cell. In summary, the clustering based ROM of woven composites was effectively implemented as a mesoscale-macroscale two-scale coupling in combination with a macroscopic yield criterion.

The present paper introduces a three-scale bridging approach, in which the macroscale response of a woven unit cell is obtained by clustering analyses and the mesoscopic responses of the yarn materials follow from a microstructural homogenization procedure. As the result, the prediction of the macroscopic response of woven composites follows from a microscale-mesoscale-macroscale bridging, accomplished by a two-step homogenization. Good captures

of the nonlinear behavior of woven composites are targeted by exploiting the strengths of two different homogenization techniques:

- The yarns microstructure can locally be treated as a UD fibrous composite. Considering the rather simple microstructure, the microscale-mesoscale transition of the yarn materials is achieved by the MFH with an incremental-secant formalism (Wu et al., 2013a).

- Piecewise uniform field ROM approaches based on micromechanical formulations allow to account for complex and anisotropic structures. Therefore, it is made use of either the TFA or a modified tangent HS for the homogenization of the complex unit cell mesostructure and the determination of the macroscopic response.

The novel three-scale bridging technique introduced in this work is built on the following ingredients:

- A mesoscale to macroscale upscaling using a clustering that bases on the varying orientation of a non-uniform, fibrous microstructure. Here, it is used as a first decomposition step of the yarns. As visible in the achieved results, this division step ensures exact elastic predictions.

- Subdomain refinements during the mesoscale to macroscale upscaling based on particular typical inelastic deformation fields in the woven unit cell. As the number of possible mesoscopic deformation fields in the woven composite unit cell, even under non-proportional loading histories, is rather low, the expected deformation fields can be well reproduced by a low number of offline stage deformation modes, provided a sensible choice of the modes. With a low number of required modes, a good representation of the emerging mesoscopic inelastic deformation patterns can be accomplished without large numbers of subdomains. Consequently, as the inelastic fields under various loading conditions can reliably be captured by limited numbers of degrees of freedom, clustering-based ROM of the mesoscale problem appears to be a suitable homogenization technique for woven composites.

- The modification of the total-secant HS type analysis (Wulfinghoff et al., 2018) towards a tangent formulation. This allows the modeling of loading histories that include loading and unloading stages.

- A re-defined concept for the mesoscopic nonlinear behavior of the subdomains of the woven unit cell, in particular of the eigenstrains required to formulate the clustering-based ROM of the mesoscale problem. Constitutive relations of the subdomains are replaced by a homogenization of the underlying microstructure using the MFH. The use of the MFH for the microscale to mesoscale upscaling allows a pre-defined yield criterion of the unit cell to be waived and enables the consideration of arbitrary inelastic loading conditions. The eigenstrains are thus redefined from a virtual unloading of the yarn response at the local mesoscale material points.

This paper is structured as follows: Section 2 outlines the analytical scale-coupling relations considered for the woven unit cell. The TFA and the Lippmann-Schwinger equation based approaches and their reduced forms used for the mesoscale to macroscale homogenization, and the yarns microstructural description and homogenization using the MFH are presented. Section 3 contains the model order reduction procedure adapted for the woven composite unit cell, through a spatial decomposition based on the local yarn orientation and inelastic fields. Moreover, details about the implementation of the modified tangent HS type analysis approach are given. Section 4 presents results from various numerical tests performed on the woven unit cell. Results of the TFA and HS ROM approaches are displayed and compared to DNS. In Section 5, concluding remarks of this work and possible future extensions of this subject, with an emphasis on the modeling of damage, are pointed out.

2. Constitutive multiscale relations in inelastic composite media

The macroscopic material domain is defined by the macroscopic material points $\boldsymbol{X}$. Since the material has an underlying heterogeneous structure, the macroscopic stress-strain response at the material point $\boldsymbol{X}$ follows from the non-uniform local responses, on the lower length scales in the material. For this sake, the macroscopic material point $\boldsymbol{X}$ is considered as the center of a bounded domain V, representative of the macroscopic material domain, with the volume

$$|V| = \int_V \mathrm{d}\boldsymbol{\chi}\,, \tag{1}$$

where $\boldsymbol{\chi}$ are the local material points. In this work about the homogenization of a woven composite, V is referred to as the mesoscopic unit cell of the woven composite, and $\boldsymbol{\chi}$ are the mesoscopic material points. The volume V consists of the material domains of the yarns, V_Y, comprising the weft yarn V_{Weft} and the warp yarn V_{Warp}, and of the pure matrix material domain V_{M}. The macroscopic, or homogenized, strain $\overline{\boldsymbol{\varepsilon}}(\boldsymbol{X})$ is the volume average of the mesoscopic strains $\boldsymbol{\varepsilon}(\boldsymbol{\chi})$ over the mesoscopic domain V:

$$\overline{\boldsymbol{\varepsilon}}(\boldsymbol{X}) = \overline{\boldsymbol{\varepsilon}} = \frac{1}{|V|}\int_V \boldsymbol{\varepsilon}(\boldsymbol{\chi})\mathrm{d}\boldsymbol{\chi}\,. \tag{2}$$

The homogenized, macroscopic stress response $\overline{\boldsymbol{\sigma}}(\boldsymbol{X})$ of the heterogeneous material body V at the macroscopic point $\boldsymbol{X}$ is equivalently expressed as

$$\overline{\boldsymbol{\sigma}}(\boldsymbol{X}) = \overline{\boldsymbol{\sigma}} = \frac{1}{|V|}\int_V \boldsymbol{\sigma}(\boldsymbol{\chi})\mathrm{d}\boldsymbol{\chi}\,, \tag{3}$$

where $\boldsymbol{\sigma}(\boldsymbol{\chi})$ are the mesoscopic stresses. In this work, this scales transition is achieved considering clustering approaches (Section 2.1).

In linear elasticity, the mesoscopic stress field $\boldsymbol{\sigma}(\boldsymbol{\chi})$ in Eq. (3) is given as

$$\boldsymbol{\sigma}(\boldsymbol{\chi}) = \mathbb{C}^{\mathrm{el}}(\boldsymbol{\chi}) : \boldsymbol{\varepsilon}(\boldsymbol{\chi}), \quad \boldsymbol{\chi} \in V, \tag{4}$$

with the mesoscopic elastic stiffness tensor $\mathbb{C}^{\mathrm{el}}(\boldsymbol{\chi}) = \partial\boldsymbol{\sigma}(\boldsymbol{\chi})/\partial\boldsymbol{\varepsilon}(\boldsymbol{\chi})$. In general, possibly nonlinear, solid media, the local (here mesoscopic) stress field $\boldsymbol{\sigma}(\boldsymbol{\chi}, t)$ at the time t follows from a constitutive model

$$\boldsymbol{\sigma}(\boldsymbol{\chi}, t) = f\big(\boldsymbol{\varepsilon}(\boldsymbol{\chi}, t), z(\boldsymbol{\chi}, t'), \forall t' \leq t\big)\,, \tag{5}$$

with the local strain field $\boldsymbol{\varepsilon}(\boldsymbol{\chi}, t)$ and the internal state variables $z(\boldsymbol{\chi}, t')$, where the dependence on the history is expressed through t' with $t' \leq t$. The nonlinear constitutive relation in Eq. (5) can be explicit, as in the case of, e.g., elasto-plasticity. In cases of underlying heterogeneous microstructures at the mesoscopic material points $\boldsymbol{\chi}$, as the case for the yarns of a woven composite, the relation in Eq. (5) can be implicit, following from a microstructural homogenization procedure. The nonlinear mechanical behavior of inelastic materials is typically accounted for by a consideration of a local eigenstrain field $\boldsymbol{\varepsilon}^*(\boldsymbol{\chi})$, or equivalently an eigenstress field $\boldsymbol{\sigma}^*(\boldsymbol{\chi}) = -\mathbb{C}^{\mathrm{el}}(\boldsymbol{\chi}) : \boldsymbol{\varepsilon}^*(\boldsymbol{\chi})$, in an elastic medium. The local strain field reads

$$\boldsymbol{\varepsilon}(\boldsymbol{\chi}) = \boldsymbol{\varepsilon}^{\mathrm{el}}(\boldsymbol{\chi}) + \boldsymbol{\varepsilon}^*(\boldsymbol{\chi}), \tag{6}$$

composed of an elastic portion $\boldsymbol{\varepsilon}^{\mathrm{el}}(\boldsymbol{\chi})$ and the eigenstrain field $\boldsymbol{\varepsilon}^*(\boldsymbol{\chi})$. The constitutive relation in Eq. (5) is alternatively stated under the form

$$\begin{aligned} \boldsymbol{\sigma}(\boldsymbol{\chi}) &= \mathbb{C}^{\mathrm{el}}(\boldsymbol{\chi}) : \big(\boldsymbol{\varepsilon}(\boldsymbol{\chi}) - \boldsymbol{\varepsilon}^*(\boldsymbol{\chi})\big) \\ &= \mathbb{C}^{\mathrm{el}}(\boldsymbol{\chi}) : \boldsymbol{\varepsilon}(\boldsymbol{\chi}) + \boldsymbol{\sigma}^*(\boldsymbol{\chi})\,, \end{aligned} \tag{7}$$

implying that the eigenstrains belong to the internal state variables $z(\boldsymbol{\chi})$ in Eq. (5).

The yarns of the woven composite are composed of elastic fibers in the same matrix material as the pure matrix phase. Therefore, in this work, the effective mesoscopic stresses $\boldsymbol{\sigma}(\boldsymbol{\chi})$ in Eq. (5), at the mesoscopic material points $\boldsymbol{\chi}$ located in the yarn domains V_Y ($Y = \mathrm{Weft}, \mathrm{Warp}$), are determined from a microstructural homogenization procedure of the yarn material (Section 2.2). The response of the inelastic matrix material of the yarns is governed by the J_2-plasticity model (Section 2.3). The eigenstrains $\boldsymbol{\varepsilon}^*(\boldsymbol{\chi})$ in the yarns V_Y follow from an elastic unloading procedure as

$$\boldsymbol{\varepsilon}^*(\boldsymbol{\chi}) = \boldsymbol{\varepsilon}(\boldsymbol{\chi}) - \big(\mathbb{C}^{\mathrm{el}}(\boldsymbol{\chi})\big)^{-1} : \boldsymbol{\sigma}(\boldsymbol{\chi})\,, \quad \forall \boldsymbol{\chi} \in V_Y\,. \tag{8}$$

In the pure matrix phase domain V_{M} of the woven composite unit cell, surrounding the yarns, the eigenstrains $\boldsymbol{\varepsilon}^*(\boldsymbol{\chi})$, computed directly as plastic strains, and the stresses $\boldsymbol{\sigma}(\boldsymbol{\chi})$ follow from the J_2-plasticity model (Section 2.3).

2.1. Scale-couplings in heterogeneous continua

According to Eq. (2), the macroscopic strain of the domain V is the volume average over the whole domain V. If the macroscopic deformation of the domain V is prescribed, a relationship between the macroscopic strain $\overline{\boldsymbol{\varepsilon}}$ and the local field $\boldsymbol{\varepsilon}(\boldsymbol{\chi})$ is required. Using computational methods like the FE, the deformation field is numerically solved over the whole domain by the computation of the local constitutive relations. The solution of the

distribution of the local strains $\boldsymbol{\varepsilon}(\boldsymbol{\chi})$ can as well be expressed by different analytical micromechanical models. In the following, two different approaches for the modeling of strain distributions inside general multi-phase media are presented: The transformation field analysis (TFA), taking into account the real underlying structure of the heterogeneous material, and the Hashin-Shtrikman (HS) type analysis, relying on the assumption of a homogeneous and isotropic reference medium. These models here provide a relationship between the macroscopic scale $\boldsymbol{X}$ and the mesoscopic fields at $\boldsymbol{\chi}$.

2.1.1. Polarization field analysis

The local strain field $\boldsymbol{\varepsilon}(\boldsymbol{\chi})$ in the domain V under homogeneous loading conditions $\overline{\boldsymbol{\varepsilon}}$ may be computed using the Lippmann-Schwinger equation

$$\boldsymbol{\varepsilon}(\boldsymbol{\chi}) = \overline{\boldsymbol{\varepsilon}} + \int_V \Gamma(\boldsymbol{\chi}, \boldsymbol{\chi}') : \boldsymbol{\tau}(\boldsymbol{\chi}') \mathrm{d}\boldsymbol{\chi}', \quad \boldsymbol{\chi}, \boldsymbol{\chi}' \in V\,, \tag{9}$$

with the polarization stress field

$$\boldsymbol{\tau}(\boldsymbol{\chi}) = \boldsymbol{\sigma}(\boldsymbol{\chi}) - \mathbb{C} : \boldsymbol{\varepsilon}(\boldsymbol{\chi}), \tag{10}$$

where $\mathbb{C}$ is the stiffness of a homogeneous reference medium, and the product $\mathbb{C} : \boldsymbol{\varepsilon}(\boldsymbol{\chi})$ represents the stress that would exist locally in the reference medium under the same local strain $\boldsymbol{\varepsilon}(\boldsymbol{\chi})$ (Kröner, 1977).

The influence of a local polarization stress field on the local strain field is expressed by means of the classical Green's operator

$$\Gamma_{ijkl} = \frac{1}{2}\left[\frac{\partial^2 G_{ik}}{\partial\chi_j \partial\chi_l} + \frac{\partial^2 G_{jk}}{\partial\chi_i \partial\chi_l}\right], \tag{11}$$

derived from the Green's function of the homogeneous reference medium $G(\boldsymbol{\chi}, \boldsymbol{\chi}')$, satisfying

$$\mathbb{C}_{ijkl} \frac{\partial^2 G_{kp}}{\partial\chi_l \partial\chi_j}(\boldsymbol{\chi}, \boldsymbol{\chi}') + \delta_{ip}\, \delta(\boldsymbol{\chi} - \boldsymbol{\chi}') = 0\,. \tag{12}$$

As the reference medium is homogeneous, the Green's interaction operator Γ is only dependent, and inversely proportional, to the stiffness of the medium:

$$\Gamma(\boldsymbol{\chi}, \boldsymbol{\chi}') \propto \mathbb{C}^{-1}\,. \tag{13}$$

In approaches by Liu et al. (2016), referred to as the Self-Consistent Clustering Analysis (SCCA), and Wulfinghoff et al. (2018), referred to as the Hashin-Shtrikman (HS) type analysis, the reference stiffness $\mathbb{C}$ is replaced by an isotropic (isotropized) reference stiffness

$$\mathbb{C} = \mathbb{C}^{\mathrm{iso}} = 3\,\kappa\,\mathbb{I}^{\mathrm{vol}} + 2\,G\,\mathbb{I}^{\mathrm{dev}}\,, \tag{14}$$

with the bulk modulus κ and the shear modulus G of the reference medium, and where

$$\mathbb{I}^{\mathrm{vol}} = \frac{1}{3}\boldsymbol{I} \otimes \boldsymbol{I}, \tag{15}$$

$$\mathbb{I}^{\mathrm{dev}} = \mathbb{I} - \mathbb{I}^{\mathrm{vol}} \tag{16}$$

and $\boldsymbol{I}$ and $\mathbb{I}$ are the second and fourth order unity tensors. During elasticity, the reference medium is assumed to have the stiffness $\mathbb{C}^{0,\mathrm{iso}}$. Once inelastic effects occur, the instantaneous response of the composite is expressed by the instantaneous isotropic stiffness $\mathbb{C}^{\mathrm{iso}}$ (Liu et al., 2016; Wulfinghoff et al., 2018). In this work, the HS type analysis by Wulfinghoff et al. (2018); Cavaliere et al. (2020) was adopted.

2.1.2. Transformation field analysis

The Transformation Field Analysis (TFA) builds on the separation of elastic fields and so-called eigenstrain (transformation strain) fields $\boldsymbol{\varepsilon}^*(\boldsymbol{\chi})$. In this work, mesoscopic eigenstrains represent the inelastic strains, following from the mesoscopic constitutive relations. Local mesoscopic strains decomposed in their elastic and inelastic contributions are formulated by Eq. (6).

If the state of the material domain V is elastic without any inelastic loading history, such that $\boldsymbol{\varepsilon}^*(\boldsymbol{\chi}) = 0,\ \forall \boldsymbol{\chi} \in V$, the local strain field $\boldsymbol{\varepsilon}(\boldsymbol{\chi})$ inside the body can be expressed as

$$\boldsymbol{\varepsilon}(\boldsymbol{\chi}) = \mathbb{A}^{\mathrm{el}}(\boldsymbol{\chi}) : \overline{\boldsymbol{\varepsilon}}, \quad \boldsymbol{\chi} \in V \tag{17}$$

with the local elastic strain concentration tensor $\mathbb{A}^{\mathrm{el}}(\boldsymbol{\chi}) = \partial\boldsymbol{\varepsilon}(\boldsymbol{\chi})/\partial\overline{\boldsymbol{\varepsilon}}$ (only if $\boldsymbol{\varepsilon}^*(\boldsymbol{\chi}) = \text{const.}, \forall \boldsymbol{\chi} \in V$), and the local stress field is given by Eq. (4). The expression of the overall strain and stress in Eqs. (2) and (3) can be reformulated to

$$\overline{\boldsymbol{\varepsilon}} = \left[\frac{1}{|V|}\int_V \mathbb{A}^{\mathrm{el}}(\boldsymbol{\chi})\,\mathrm{d}\boldsymbol{\chi}\right] : \overline{\boldsymbol{\varepsilon}} \tag{18}$$

and

$$\overline{\boldsymbol{\sigma}} = \left[\frac{1}{|V|}\int_V \mathbb{C}^{\mathrm{el}}(\boldsymbol{\chi}) : \mathbb{A}^{\mathrm{el}}(\boldsymbol{\chi})\,\mathrm{d}\boldsymbol{\chi}\right] : \overline{\boldsymbol{\varepsilon}}, \tag{19}$$

the latter leading to the expression for the overall elastic stiffness

$$\begin{aligned} \overline{\mathbb{C}}^{\mathrm{el}} &= \frac{\partial\overline{\boldsymbol{\sigma}}}{\partial\overline{\boldsymbol{\varepsilon}}}, \quad \text{at } \boldsymbol{\varepsilon}^*(\boldsymbol{\chi}) = \text{const.},\ \forall \boldsymbol{\chi} \in V \\ &= \frac{1}{|V|}\int_V \mathbb{C}^{\mathrm{el}}(\boldsymbol{\chi}) : \mathbb{A}^{\mathrm{el}}(\boldsymbol{\chi})\mathrm{d}\boldsymbol{\chi}. \end{aligned} \tag{20}$$

In the case of an eigenstrain field $\boldsymbol{\varepsilon}^*(\boldsymbol{\chi})$ and a vanishing overall strain $\overline{\boldsymbol{\varepsilon}} = 0$, the local strain field can be expressed as

$$\boldsymbol{\varepsilon}(\boldsymbol{\chi}) = \mathbb{D}(\boldsymbol{\chi}, \boldsymbol{\chi}') : \boldsymbol{\varepsilon}^*(\boldsymbol{\chi}') \quad \boldsymbol{\chi}, \boldsymbol{\chi}' \in V\,, \tag{21}$$

with the interaction function $\mathbb{D}(\boldsymbol{\chi}, \boldsymbol{\chi}')$, estimating the effect of an eigenstrain field $\boldsymbol{\varepsilon}^*(\boldsymbol{\chi}')$ on the strain at $\boldsymbol{\chi}$ (Dvorak, 1992). The superposition of the two Eqs. (17) and (21) provides the TFA two-scale coupling relation

$$\boldsymbol{\varepsilon}(\boldsymbol{\chi}) = \mathbb{A}^{\mathrm{el}}(\boldsymbol{\chi}) : \overline{\boldsymbol{\varepsilon}} + \mathbb{D}(\boldsymbol{\chi}, \boldsymbol{\chi}') : \boldsymbol{\varepsilon}^*(\boldsymbol{\chi}'), \quad \boldsymbol{\chi}, \boldsymbol{\chi}' \in V. \tag{22}$$

2.1.3. Discretized consideration of subdomains

The scale-coupling formulations presented in Sections 2.1.1 and 2.1.2 can be reduced considering a division of the domain V into subdomains V_r. Average quantities over the subdomains with the volumes

$$|V_r| = \int_{V_r} \mathrm{d}\boldsymbol{\chi} \tag{23}$$

are considered instead of local quantities and a uniform distribution of all internal state variables is assumed inside the K subdomains denoted by the index r. The piecewise uniform fields of local variables $\beta(\boldsymbol{\chi})$, where $\beta = \boldsymbol{\varepsilon}, \boldsymbol{\varepsilon}^*, \boldsymbol{\sigma}$, are expressed by

$$\beta(\boldsymbol{\chi}) = \sum_{r=1}^{K} \beta_r \xi_r(\boldsymbol{\chi}) \tag{24}$$

with the per-subdomain V_r constant value β_r and the spatial distribution function

$$\xi_r(\boldsymbol{\chi}) = \begin{cases} 1 & \text{, if } \boldsymbol{\chi} \in V_r \\ 0 & \text{, otherwise.} \end{cases} \tag{25}$$

It follows

$$\beta_r = \frac{1}{|V_r|} \int_{V_r} \beta(\boldsymbol{\chi}) \mathrm{d}\boldsymbol{\chi}\,, \tag{26}$$

meaning that the uniform quantities of a subdomain equal the quantities averaged over the subdomain. The homogenized macroscopic strain and stress can now be expressed as

$$\overline{\boldsymbol{\varepsilon}} = \sum_{r=1}^{K} \upsilon_r \boldsymbol{\varepsilon}_r, \tag{27}$$

and

$$\overline{\boldsymbol{\sigma}} = \sum_{r=1}^{K} \upsilon_r \boldsymbol{\sigma}_r, \tag{28}$$

where $\upsilon_r = |V_r|/|V|$ is the volume fraction of the subdomain V_r. The subdomain stresses $\boldsymbol{\sigma}_r$, the algorithmic tangent operator

$$\mathbb{C}_r^{\mathrm{alg}} = \frac{\partial \Delta \boldsymbol{\sigma}_r}{\partial \boldsymbol{\varepsilon}_r}, \tag{29}$$

the eigenstrain $\boldsymbol{\varepsilon}_r^*$ and its derivative $\partial \Delta \boldsymbol{\varepsilon}_r^* / \partial \boldsymbol{\varepsilon}_r$, are all assumed uniform per-subdomain. If the subdomain V_r is located in the pure matrix phase domain V_{M}, the quantities $\boldsymbol{\sigma}_r$, $\mathbb{C}_r^{\mathrm{alg}}$, $\boldsymbol{\varepsilon}_r^*$ follow from the J_2-plasticity model (Section 2.3). If the domain V_r is located in one of the yarn domains V_Y, possessing an underlying composite microstructure, $\boldsymbol{\sigma}_r$ and $\mathbb{C}_r^{\mathrm{alg}}$ are computed from a homogenization procedure of the associated microstructure with the effective microstructural configuration (Section 2.2). The eigenstrains of the yarn subdomains, $\boldsymbol{\varepsilon}_r^*$, follow from the elastic unloading as

$$\boldsymbol{\varepsilon}_r^* = \boldsymbol{\varepsilon}_r - (\mathbb{C}_r^{\mathrm{el}})^{-1} : \boldsymbol{\sigma}_r\,. \tag{30}$$

In the following, the TFA and HS algorithms are formulated incrementally, with the rates of the quantities β integrated over a discrete time interval denoted as increments $\Delta\beta$. The TFA formulation in Eq. (22) is stated in its reduced form as

$$\Delta\boldsymbol{\varepsilon}_r = \mathbb{A}_r^{\mathrm{el}} : \Delta\overline{\boldsymbol{\varepsilon}} + \sum_{s=1}^{K} \mathbb{D}_{rs} : \Delta\boldsymbol{\varepsilon}_s^* \,, \tag{31}$$

with the subdomains average strain concentration tensors $\mathbb{A}_r^{\mathrm{el}}$ and the interaction tensors $\mathbb{D}_{rs}$ between two subdomains. The reduced incremental form of the HS algorithm in Eq. (9) using subdomains is expressed as

$$\Delta\boldsymbol{\varepsilon}_r = \Delta\overline{\boldsymbol{\varepsilon}} + \sum_{s=1}^{K} \Gamma_{rs} : \Delta\boldsymbol{\tau}_s = \Delta\overline{\boldsymbol{\varepsilon}} + \sum_{s=1}^{K} \Gamma_{rs} : \left(\Delta\boldsymbol{\sigma}_s - \mathbb{C}^{\mathrm{iso}} : \Delta\boldsymbol{\varepsilon}_s\right) \tag{32}$$

with the Green's interaction tensors between two subdomains Γ_{rs}.

2.2. Mesoscopic constitutive relations: homogenization of the yarn material

The yarn material consists of longitudinal fibers in the yarn direction embedded in the matrix material. Accordingly, each mesoscopic material point $\boldsymbol{\chi}$ or each mesoscopic subdomain V_r located inside one of the yarns, is constituted by a microstructural two-phase composite medium, consisting of an inclusion (fiber) phase (subscript II) embedded in a matrix (subscript I). The mesoscopic material point $\boldsymbol{\chi}$ and the mesoscopic subdomains V_r are represented by associated microstructural RVEs, which represent the local, or subdomains, underlying microstructure. The microstructural RVE contains the two material phases with the phase volume ratios $v_{\mathrm{I}}(\boldsymbol{\chi})$ and $v_{\mathrm{II}}(\boldsymbol{\chi})$, or v_{I_r} and v_{II_r}, where

$$v_{\mathrm{I}} + v_{\mathrm{II}} = 1 \,, \tag{33}$$

and where, in all generalities the local volume fractions of the material phases can be non-uniform and thus depend on the mesoscale material point $\boldsymbol{\chi}$ or on the mesoscopic subdomain V_r. Homogenized responses at the mesoscopic material point $\boldsymbol{\chi}$, or of the mesoscopic subdomain V_r with uniform fields of variables, are computed from a microstructural homogenization procedure using the Mean Field Homogenization (MFH) technique.

2.2.1. Microstructural definition

In MFH approaches, the microstructural two-phase composite medium is represented by an RVE that contains an equivalent two-phase medium, consisting of one equivalent inclusion embedded in the matrix, or host, phase. The equivalent inclusion in the RVE is representative of the actual microstructural configuration of the inclusion phase. The matrix (host) phase and the inclusion phase are represented by uniform fields of variables with average quantities. The homogenized response of the microstructural RVE depends on the geometry information of the two-phase system in the RVE. With an isotropic host phase, the local geometrical information is expressed by $g_{\mathrm{II}}(\boldsymbol{\chi})$, containing the aspect ratio and spatial orientation of the local equivalent inclusion at $\boldsymbol{\chi}$.

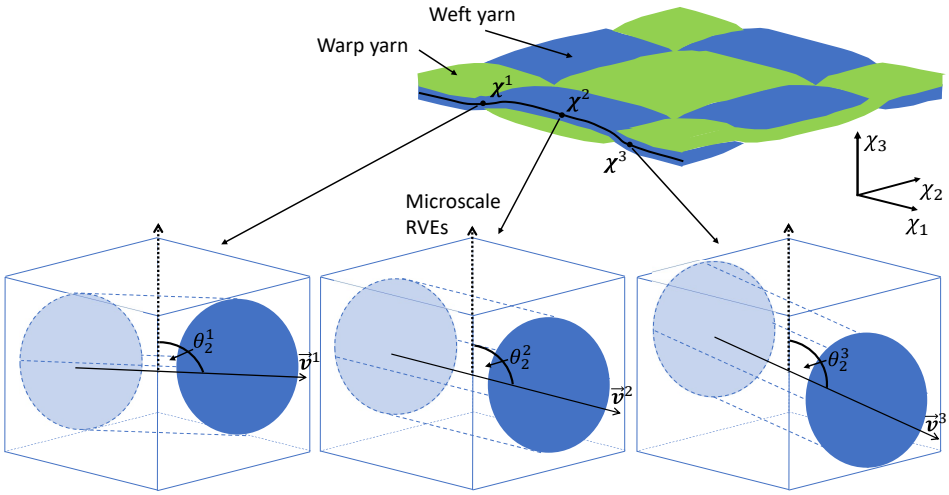

Figure 2: Schematic representation of the mesoscopic woven unit cell, built by the weft (blue) and warp (green) yarns, and of the yarns microstructure. A simplified representation of the yarns fibrous microstructure is provided by the microscale RVEs, locally consisting of one equivalent UD fiber in the matrix (Section 2.2.1). The inclination of the yarns leads to locally varying fiber orientations. The varying yarn/fiber orientations imply the consideration of different microscale RVEs, as displayed, where the fiber has different inclination angles. The yarn/fiber inclinations at three different locations $\boldsymbol{\chi}^i$ in the weft yarn are indicated by the corresponding second Euler angles $\theta_2^i(\boldsymbol{\chi}^i)$, and fiber directions are denoted by the vector $\vec{v}^i(\boldsymbol{\chi}^i)$ (Eq. (35)).

Here, the local equivalent elliptical inclusion represents uni-directional fibers, and so the ellipse aspect ratio is very large and considered uniform in the yarn material. The local orientation of the fibers, however, varies according to the local yarn inclination. Consequently, the mesoscopic material points $\boldsymbol{\chi}$ in the yarns are represented by microstructural RVEs with varying inclusion orientations, corresponding to the local yarn/fiber orientation at $\boldsymbol{\chi}$ (Fig. 2). The non-uniform orientation of the RVE inclusion is characterized by the local Euler angles $\theta(\boldsymbol{\chi}) = \big(\theta_1(\boldsymbol{\chi}),\, \theta_2(\boldsymbol{\chi}),\, \theta_3(\boldsymbol{\chi})\big)$, describing the orientation of the local rotated coordinate system χ_1, χ_2, χ_3 spanned by the rotated eigenvectors $\vec{e}_1'', \vec{e}_2'', \vec{e}_3''$, with respect to the global coordinate system χ_1, χ_2, χ_3, spanned by the global eigenvectors $\vec{e}_1, \vec{e}_2, \vec{e}_3$ of the unit cell reference system. If $\theta(\boldsymbol{\chi}) = (0°, 0°, 0°)$, the rotated system equals the global system. Before the rotation, the fibers align with the global χ_3-axis, with the orientation expressed by the unit vector $\vec{e}_3$. After the full rotation, they align with the locally rotated χ_3''-axis, expressed by the unit vector $\vec{e}_3''$.

With the fibers following the weft and warp yarns oriented in the global χ_1- and χ_2-axis directions, respectively, the first Euler angle (rotation $Q_1\big(\theta_1(\boldsymbol{\chi})\big)$ around the global χ_3-axis) is given as

$$\theta_1(\boldsymbol{\chi}) = \begin{cases} 90° & , \boldsymbol{\chi} \in V_{\text{Weft}} \\ 0° & , \boldsymbol{\chi} \in V_{\text{Warp}}\,. \end{cases} \tag{34}$$

The second Euler angle (rotation $Q_2\big(\theta_2(\boldsymbol{\chi})\big)$ around rotated χ_1'-axis) represents the local vertical inclination of the yarn in which $\boldsymbol{\chi}$ is located, where $\theta_2(\boldsymbol{\chi}) = 90°$ means a perfectly

horizontal alignment (see in Fig. 2). In the locations of upwards and downwards inclination of the yarns, the second Euler takes the values $\theta_2(\boldsymbol{\chi}) = 76°$ and $\theta_2(\boldsymbol{\chi}) = 104°$, respectively, see Section 4, meaning that $76° \leq \theta_2(\boldsymbol{\chi}) \leq 104°$. The third euler angle (rotation around rotated χ_3''-axis) is of no importance for the local fiber orientation. In conclusion, the local fiber orientation at the location $\boldsymbol{\chi}$ may be expressed by

$$\vec{v}(\boldsymbol{\chi}) = \vec{e}_3'' = Q_2\big(\theta_2(\boldsymbol{\chi})\big) \cdot Q_1\big(\theta_1(\boldsymbol{\chi})\big) \cdot \vec{e}_3 = Q(\boldsymbol{\chi}) \cdot \vec{e}_3\,, \tag{35}$$

where $Q(\boldsymbol{\chi}) = Q\big(\theta_1(\boldsymbol{\chi}), \theta_2(\boldsymbol{\chi})\big)$ is the total local rotation from the global eigenvector $\vec{e}_3$ towards the local fiber orientation at $\boldsymbol{\chi}$. Details on the rotations are given in Appendix A.

Considering the spatial subdomain decomposition (Section 2.1.3), the subdomains V_r, composed by the mesoscopic material points $\boldsymbol{\chi} \in V_r$, are represented by an associated effective microstructural RVE. The effective geometry of the equivalent inclusion g_{II_r} of the subdomain V_r is characterized by the homogenized euler angles $\theta_r = \big(\theta_{1_r}, \theta_{2_r}\big)$. The homogenized Euler angles, representing the effective inclusion orientation for the subdomain V_r, are computed as the circular mean following

$$\theta_r = \frac{1}{2}\arctan(A/B)\,, \tag{36}$$

where

$$A = \frac{1}{|V_r|}\int_{V_r} \sin\big(2\theta(\boldsymbol{\chi})\big)\mathrm{d}\boldsymbol{\chi} \tag{37}$$

and

$$B = \frac{1}{|V_r|}\int_{V_r} \cos\big(2\theta(\boldsymbol{\chi})\big)\mathrm{d}\boldsymbol{\chi}\,, \tag{38}$$

and the factor two is required for the correct computation of the mean orientation. The Eqs. (36), (37) and (38) are applied for the homogenization of each component of θ_r. The subdomain fiber orientation is expressed as

$$\vec{v}_r = Q_2\big(\theta_{2_r}\big) \cdot Q_1\big(\theta_{1_r}\big) \cdot \vec{e}_3 = Q(\theta_{1_r}, \theta_{2_r}) \cdot \vec{e}_3\,. \tag{39}$$

As already mentioned, each mesoscopic material point $\boldsymbol{\chi}$ and each subdomain V_r are constituted by a microstructural composite medium of the two phases I, II. In the following equations and subsections Sections 2.2.2 and 2.2.3, the material point denoted by $\boldsymbol{\chi}$ and the subscript r referring to the subdomain are omitted. The homogenized strains at the mesoscopic material points $\boldsymbol{\chi}$, $\boldsymbol{\varepsilon}(\boldsymbol{\chi})$, or the strains of the mesoscopic subdomains, $\boldsymbol{\varepsilon}_r$, are expressed as

$$\boldsymbol{\varepsilon} = \upsilon_{\mathrm{I}}\boldsymbol{\varepsilon}_{\mathrm{I}} + \upsilon_{\mathrm{II}}\boldsymbol{\varepsilon}_{\mathrm{II}}\,, \tag{40}$$

where $\boldsymbol{\varepsilon}_{\mathrm{I}}$ and $\boldsymbol{\varepsilon}_{\mathrm{II}}$ are the strains of the two phases in the microstructural RVE.

2.2.2. Incremental-secant Mori-Tanaka MFH scheme

The distribution of the strains in Eq. (40) using MFH approaches is governed by certain localization rules. In this paper, the strain localization tensor introduced by Mori and Tanaka (1973) is considered, linking the strain distribution in both microstructural phases. The incremental strain distribution, using the Mori-Tanaka (MT) MFH scheme, is expressed by the strain localization tensor

$$\mathbb{B}_{\mathrm{II}} = f(g_{\mathrm{II}}, \mathbb{C}_{\mathrm{I}}^{\mathrm{LCC}}, \mathbb{C}_{\mathrm{II}}^{\mathrm{LCC}}) \,, \tag{41}$$

where $\mathbb{C}_{\mathrm{I}}^{\mathrm{LCC}}$ and $\mathbb{C}_{\mathrm{II}}^{\mathrm{LCC}}(g_{\mathrm{II}})$ are the so-called linear comparison operators of the phases. The strain localization tensor $\mathbb{B}_{\mathrm{II}}$ provides the link between the occurring strains in each of the two material phases and is expressed as

$$\mathbb{B}_{\mathrm{II}} = \{\mathbb{I} + \mathbb{S} : [(\mathbb{C}_{\mathrm{I}}^{\mathrm{LCC}})^{-1} : \mathbb{C}_{\mathrm{II}}^{\mathrm{LCC}} - \mathbb{I}]\}^{-1} \,, \tag{42}$$

with the fourth order unity tensor $\mathbb{I}$, the Eshelby tensor $\mathbb{S}(g_{\mathrm{II}}, \mathbb{C}_{\mathrm{I}}^{\mathrm{LCC}})$, depending on the inclusion geometry g_{II} and the stiffness operator of the host phase $\mathbb{C}_{\mathrm{I}}^{\mathrm{LCC}}$. During linear elastic deformation of the composite, the linear comparison stiffnesses of the phases are given as the constant elastic stiffnesses of the phases: $\mathbb{C}_{\mathrm{I}}^{\mathrm{LCC}} = \mathbb{C}_{\mathrm{I}}^{\mathrm{el}}$, $\mathbb{C}_{\mathrm{II}}^{\mathrm{LCC}} = \mathbb{C}_{\mathrm{II}}^{\mathrm{el}}$. The strains in the two phases during linear elastic deformation are linked by the expression

$$\boldsymbol{\varepsilon}_{\mathrm{II}} = \mathbb{B}_{\mathrm{II}}^{\mathrm{el}} : \boldsymbol{\varepsilon}_{\mathrm{I}} \,, \tag{43}$$

with the constant elastic localization tensor

$$\mathbb{B}_{\mathrm{II}}^{\mathrm{el}} = \{\mathbb{I} + \mathbb{S} : [(\mathbb{C}_{\mathrm{I}}^{\mathrm{el}})^{-1} : \mathbb{C}_{\mathrm{II}}^{\mathrm{el}} - \mathbb{I}]\}^{-1} \,. \tag{44}$$

During inelastic loading, the instantaneous stiffnesses of the phase deviate from their elastic stiffnesses, and therefore, $\mathbb{B}_{\mathrm{II}} \neq \mathbb{B}_{\mathrm{II}}^{\mathrm{el}}$. In this work, the incremental-secant MFH formulation is chosen (Wu et al., 2013a), where the strain distribution in the two phases is controlled by the incremental secant stiffnesses of the phases $\mathbb{C}_{\mathrm{I}}^{\mathrm{sec}}$ and $\mathbb{C}_{\mathrm{II}}^{\mathrm{sec}}$. The choice for the incremental-secant formalism stems from the observation that the prediction of inelastic material behaviors under non-proportional loading conditions could be clearly improved with respect to, e.g., the tangent MFH formalism (Wu et al., 2013a). Subject of the incremental secant formulation are so-called strain reloading increments $\Delta\boldsymbol{\varepsilon}_{\mathrm{I}}^{\mathrm{re}}$ and $\Delta\boldsymbol{\varepsilon}_{\mathrm{II}}^{\mathrm{re}}$, describing the loading from a computed residual state towards the new state (Section 2.2.3, Fig. 3), and linked by the incremental-secant strain localization tensor $\mathbb{B}_{\mathrm{II}}^{\mathrm{sec}} = f(g_{\mathrm{II}}, \mathbb{C}_{\mathrm{I}}^{\mathrm{sec}}, \mathbb{C}_{\mathrm{II}}^{\mathrm{sec}})$. The relation between the matrix and the inclusion strain reloading increments is expressed following

$$\Delta\boldsymbol{\varepsilon}_{\mathrm{II}}^{\mathrm{re}} = \mathbb{B}_{\mathrm{II}}^{\mathrm{sec}} : \Delta\boldsymbol{\varepsilon}_{\mathrm{I}}^{\mathrm{re}} \,, \tag{45}$$

with

$$\mathbb{B}_{\mathrm{II}}^{\mathrm{sec}} = \{\mathbb{I} + \mathbb{S} : [(\mathbb{C}_{\mathrm{I}}^{\mathrm{sec}})^{-1} : \mathbb{C}_{\mathrm{II}}^{\mathrm{sec}} - \mathbb{I}]\}^{-1} \tag{46}$$

and the Eshelby tensor $\mathbb{S}(g_{\mathrm{II}}, \mathbb{C}_{\mathrm{I}}^{\mathrm{sec}})$. The homogenization of the reloading strain is expressed as

$$\Delta\boldsymbol{\varepsilon}^{\mathrm{re}} = v_{\mathrm{I}}\Delta\boldsymbol{\varepsilon}_{\mathrm{I}}^{\mathrm{re}} + v_{\mathrm{II}}\Delta\boldsymbol{\varepsilon}_{\mathrm{II}}^{\mathrm{re}} \,. \tag{47}$$

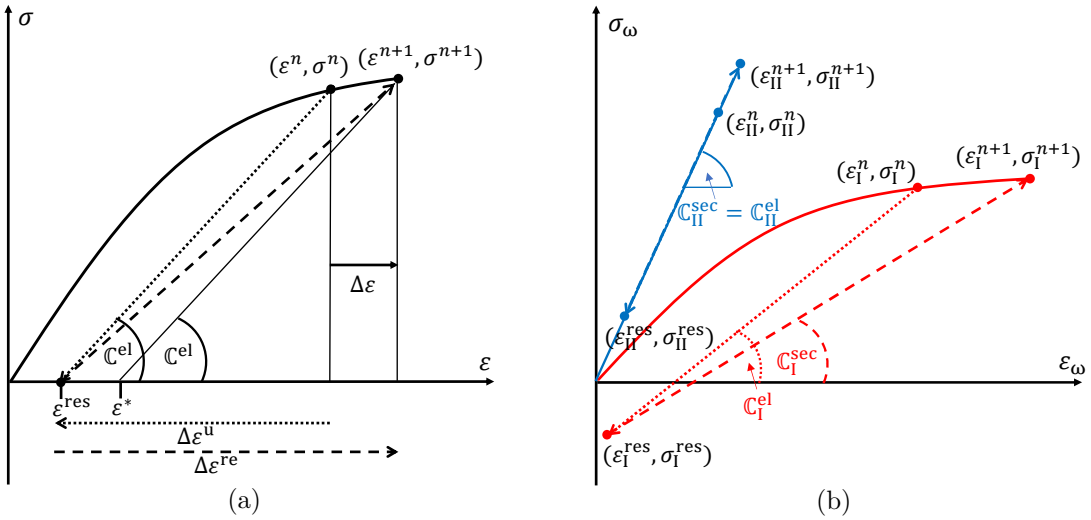

Figure 3: MFH procedure under an applied strain increment $\Delta\boldsymbol{\varepsilon}$ schematically for a two-phase composite, consisting of an elastic inclusion in an inelastic matrix: The (a) unloading-reloading procedure of the composite towards a zero-stress state (dotted) and to the new homogenized state (dashed), and (b) the unloading-reloading step translated to the two separate composite phases.

2.2.3. Incremental-secant MFH procedure: constituents and homogenized response

The homogenized mesoscopic stresses $\boldsymbol{\sigma}$ and eigenstrains $\boldsymbol{\varepsilon}^*$ follow from the virtual unloading-reloading procedure of the two-phase medium, performed at every time step (Fig. 3). First, the medium is virtually unloaded to a homogenized zero-stress state $\boldsymbol{\sigma}^{\mathrm{res}} = 0$ (Fig. 3(a)). The elastic unloading step is expressed as

$$(\boldsymbol{\varepsilon}^n, \boldsymbol{\sigma}^n) \xrightarrow{(\Delta\boldsymbol{\varepsilon}^{\mathrm{u}}, \Delta\boldsymbol{\sigma}^{\mathrm{u}})} (\boldsymbol{\varepsilon}^{\mathrm{res}}, 0)\,, \tag{48}$$

where the superscript "n" denotes the previous time-step, $\Delta\boldsymbol{\varepsilon}^{\mathrm{u}}$ and $\Delta\boldsymbol{\sigma}^{\mathrm{u}}$ are the homogenized strain and stress unloading increments, and $\boldsymbol{\varepsilon}^{\mathrm{res}}$ is the composite strain at the virtually unloaded state. As visible in Eq. (48), the composite unloading stress increment is given by $\Delta\boldsymbol{\sigma}^{\mathrm{u}} = -\boldsymbol{\sigma}^n$, and since an elastic unloading is considered, the composite unloading strain increment follows as

$$\Delta\boldsymbol{\varepsilon}^{\mathrm{u}} = (\mathbb{C}^{\mathrm{el}})^{-1} : \Delta\boldsymbol{\sigma}^{\mathrm{u}} = -(\mathbb{C}^{\mathrm{el}})^{-1} : \boldsymbol{\sigma}^n\,, \tag{49}$$

with the homogenized elastic stiffness $\mathbb{C}^{\mathrm{el}}$ (more details given in Appendix B), leading to the composite residual strain

$$\boldsymbol{\varepsilon}^{\mathrm{res}} = \boldsymbol{\varepsilon}^n - (\mathbb{C}^{\mathrm{el}})^{-1} : \boldsymbol{\sigma}^n\,. \tag{50}$$

As the composite is virtually unloaded, the material phases, denoted by the subscript $\omega \in \mathrm{I}, \mathrm{II}$, experience the virtual elastic unloading step

$$(\boldsymbol{\varepsilon}_\omega^n, \boldsymbol{\sigma}_\omega^n) \xrightarrow{(\Delta\boldsymbol{\varepsilon}_\omega^{\mathrm{u}}, \Delta\boldsymbol{\sigma}_\omega^{\mathrm{u}})} (\boldsymbol{\varepsilon}_\omega^{\mathrm{res}}, \boldsymbol{\sigma}_\omega^{\mathrm{res}})\,, \tag{51}$$

with the unloading strain and stress increments $\Delta\boldsymbol{\varepsilon}_\omega^{\mathrm{u}}$ and $\Delta\boldsymbol{\sigma}_\omega^{\mathrm{u}} = \mathbb{C}_\omega^{\mathrm{el}} : \Delta\boldsymbol{\varepsilon}_\omega^{\mathrm{u}}$ towards the residual strains and stresses $\boldsymbol{\varepsilon}_\omega^{\mathrm{res}} = \boldsymbol{\varepsilon}_\omega^{n} + \Delta\boldsymbol{\varepsilon}_\omega^{\mathrm{u}}$ and $\boldsymbol{\sigma}_\omega^{\mathrm{res}} = \boldsymbol{\sigma}_\omega^{n} + \Delta\boldsymbol{\sigma}_\omega^{\mathrm{u}}$ (Fig. 3(b)). Unlike in the homogenized consideration of the composite, the residual stress states of the single phases $\boldsymbol{\sigma}_\omega^{\mathrm{res}}$ do not necessarily equal a zero stress state. The phases unloading strain increments are solved using the elastic mean field localization rule in Eq. (43) as

$$\Delta\boldsymbol{\varepsilon}_{\mathrm{II}}^{\mathrm{u}} = \mathbb{B}_{\mathrm{II}}^{\mathrm{el}} : \Delta\boldsymbol{\varepsilon}_{\mathrm{I}}^{\mathrm{u}} \,, \tag{52}$$

together with the conditions $\Delta\boldsymbol{\varepsilon}^{\mathrm{u}} = v_{\mathrm{I}}\Delta\boldsymbol{\varepsilon}_{\mathrm{I}}^{\mathrm{u}} + v_{\mathrm{II}}\Delta\boldsymbol{\varepsilon}_{\mathrm{II}}^{\mathrm{u}}$ and $\boldsymbol{\sigma}^{\mathrm{res}} = v_{\mathrm{I}}\boldsymbol{\sigma}_{\mathrm{I}}^{\mathrm{res}} + v_{\mathrm{II}}\boldsymbol{\sigma}_{\mathrm{II}}^{\mathrm{res}} = 0$. The reloading increment towards the new state of the composite at the time step "$n+1$" is represented by

$$(\boldsymbol{\varepsilon}^{\mathrm{res}}, 0) \xrightarrow{(\Delta\boldsymbol{\varepsilon}^{\mathrm{re}}, \Delta\boldsymbol{\sigma}^{\mathrm{re}})} (\boldsymbol{\varepsilon}^{n+1}, \boldsymbol{\sigma}^{n+1}) \,, \tag{53}$$

where $\Delta\boldsymbol{\varepsilon}^{\mathrm{re}}$ is the strain and $\Delta\boldsymbol{\sigma}^{\mathrm{re}}$ the stress reloading increment (Fig. 3(a)). The composite constituents are, as the composite is reloaded according to Eq. (53), reloaded simultaneously (Fig. 3(b)) following

$$(\boldsymbol{\varepsilon}_\omega^{\mathrm{res}}, \boldsymbol{\sigma}_\omega^{\mathrm{res}}) \xrightarrow{(\Delta\boldsymbol{\varepsilon}_\omega^{\mathrm{re}}, \Delta\boldsymbol{\sigma}_\omega^{\mathrm{re}})} (\boldsymbol{\varepsilon}_\omega^{n+1}, \boldsymbol{\sigma}_\omega^{n+1}) \,. \tag{54}$$

Phase strains and stresses at the time step "$n+1$" are given as

$$\boldsymbol{\varepsilon}_\omega = \boldsymbol{\varepsilon}_\omega^{\mathrm{res}} + \Delta\boldsymbol{\varepsilon}_\omega^{\mathrm{re}} \tag{55a}$$

$$\boldsymbol{\sigma}_\omega = \boldsymbol{\sigma}_\omega^{\mathrm{res}} + \Delta\boldsymbol{\sigma}_\omega^{\mathrm{re}} \,. \tag{55b}$$

For the matrix subdomains, the zero-residual incremental-secant approach was adopted (Wu et al., 2013a), meaning that the residual stress in Eqs. (54) and (55) is neglected: $\boldsymbol{\sigma}_{\mathrm{I}}^{\mathrm{res}} = 0$. The reloading step is then performed from the zero stress state towards the new stress state. The distribution of the phases reloading strains $\Delta\boldsymbol{\varepsilon}_\omega^{\mathrm{re}}$ is solved by the MFH algorithm in Eqs. (45) and (46) based on the incremental secant phase stiffnesses $\mathbb{C}_\omega^{\mathrm{sec}}$ together with the condition in Eq. (47). The matrix and inclusions phases secant operators and reloading stresses

$$\boldsymbol{\sigma}_{\mathrm{I}} = \Delta\boldsymbol{\sigma}_{\mathrm{I}}^{\mathrm{re}} = \mathbb{C}_{\mathrm{I}}^{\mathrm{sec}} : \Delta\boldsymbol{\varepsilon}_{\mathrm{I}}^{\mathrm{re}} \quad \text{and} \quad \boldsymbol{\sigma}_{\mathrm{II}} = \boldsymbol{\sigma}_{\mathrm{II}}^{\mathrm{res}} + \Delta\boldsymbol{\sigma}_{\mathrm{II}}^{\mathrm{re}} = \boldsymbol{\sigma}_{\mathrm{II}}^{\mathrm{res}} + \mathbb{C}_{\mathrm{II}}^{\mathrm{sec}} : \Delta\boldsymbol{\varepsilon}_{\mathrm{II}}^{\mathrm{re}} \tag{56}$$

are computed from the phases constitutive relations (Section 2.3). The detailed resolution of the incremental-secant algorithm is presented by (Wu et al., 2013a).

The homogenized mesoscopic stress in Eq. (53) follows from the microstructural phase stresses in Eq. (55b) as

$$\boldsymbol{\sigma} = v_{\mathrm{I}}\boldsymbol{\sigma}_{\mathrm{I}} + v_{\mathrm{II}}\boldsymbol{\sigma}_{\mathrm{II}} \,. \tag{57}$$

The homogenized mesoscopic eigenstrain results, as visible in Fig. 3(a), in

$$\boldsymbol{\varepsilon}^* = \boldsymbol{\varepsilon} - (\mathbb{C}^{\mathrm{el}})^{-1} : \boldsymbol{\sigma} \,. \tag{58}$$

A comparison of Eqs. (50) and (58) shows that the homogenized residual strain at the following time step is equal to the homogenized eigenstrain at the current time step. The

homogenized algorithmic tangent stiffness $\mathbb{C}^{\mathrm{alg}} = \partial\boldsymbol{\sigma}/\partial\boldsymbol{\varepsilon}$, following from Eq. (57), is expressed as

$$\mathbb{C}^{\mathrm{alg}} = \upsilon_{\mathrm{I}} \frac{\partial \boldsymbol{\sigma}_{\mathrm{I}}}{\partial \boldsymbol{\varepsilon}_{\mathrm{I}}} : \frac{\partial \boldsymbol{\varepsilon}_{\mathrm{I}}}{\partial \boldsymbol{\varepsilon}} + \upsilon_{\mathrm{II}} \frac{\partial \boldsymbol{\sigma}_{\mathrm{II}}}{\partial \boldsymbol{\varepsilon}_{\mathrm{II}}} : \frac{\partial \boldsymbol{\varepsilon}_{\mathrm{II}}}{\partial \boldsymbol{\varepsilon}} \,. \tag{59}$$

Computation details are presented in Appendix C.

2.3. Microscopic constitutive relations: J_2-plasticity model

The inclusion phase $\omega = \mathrm{II}$ in this work is represented by elastic fibers, meaning that $\mathbb{C}^{\mathrm{sec}}_{\mathrm{II}} = \mathbb{C}^{\mathrm{alg}}_{\mathrm{II}} = \mathbb{C}^{\mathrm{el}}_{\mathrm{II}}$ and therefore $\boldsymbol{\sigma}_{\mathrm{II}} = \mathbb{C}^{\mathrm{el}}_{\mathrm{II}} : \boldsymbol{\varepsilon}_{\mathrm{II}}$, where $\mathbb{C}^{\mathrm{el}}_{\mathrm{II}}$ is the anisotropic elastic stiffness of the fibers. The local non-linear stress-strain response of the inelastic matrix phase $\omega = \mathrm{I}$ during the incremental secant reloading procedure Eq. (56), given by

$$\boldsymbol{\varepsilon}_{\mathrm{I}} = \boldsymbol{\varepsilon}^{\mathrm{res}}_{\mathrm{I}} + \Delta\boldsymbol{\varepsilon}^{\mathrm{re}}_{\mathrm{I}} \tag{60a}$$

$$\boldsymbol{\sigma}_{\mathrm{I}} = \Delta\boldsymbol{\sigma}^{\mathrm{re}}_{\mathrm{I}} \,, \tag{60b}$$

is governed by the J_2-plasticity model. The matrix phase is isotropic and therefore, its stiffness can be expressed as

$$\mathbb{C}^{\mathrm{el}}_{\mathrm{I}} = 3\kappa^{\mathrm{el}}_{\mathrm{I}} \mathbb{I}^{\mathrm{vol}} + 2G^{\mathrm{el}}_{\mathrm{I}} \mathbb{I}^{\mathrm{dev}} \,, \tag{61}$$

with the materials elastic bulk modulus $\kappa^{\mathrm{el}}_{\mathrm{I}}$ and shear modulus $G^{\mathrm{el}}_{\mathrm{I}}$. In the following, the common convention for equivalent strains and von Mises equivalent stresses is used for the strain and stress tensors, respectively:

$$\varepsilon^{\mathrm{eq}} = \sqrt{\frac{2}{3} \operatorname{dev}(\boldsymbol{\varepsilon}) : \operatorname{dev}(\boldsymbol{\varepsilon})} \tag{62a}$$

$$\sigma^{\mathrm{eq}} = \sqrt{\frac{3}{2} \operatorname{dev}(\boldsymbol{\sigma}) : \operatorname{dev}(\boldsymbol{\sigma})} \,. \tag{62b}$$

A radial return mapping algorithm corrects the elastic trial stress state back towards the current yield surface by computing the occurring plastic flow, so that the yield function for isotropic hardening $f^{\mathrm{Y}}(\boldsymbol{\sigma}_{\mathrm{I}}, p_{\mathrm{I}})$ satisfies

$$f^{\mathrm{Y}}(\boldsymbol{\sigma}_{\mathrm{I}}, p_{\mathrm{I}}) = \sigma^{\mathrm{eq}}_{\mathrm{I}} - \sigma^{\mathrm{Y0}}_{\mathrm{I}} - R(p_{\mathrm{I}}) \leq 0 \,, \tag{63}$$

with the equivalent stress $\sigma^{\mathrm{eq}}_{\mathrm{I}}$, the initial yield stress $\sigma^{\mathrm{Y0}}_{\mathrm{I}}$, the hardening stress $R(p_{\mathrm{I}})$, and the equivalent accumulated plastic strain p_{I}, as the time integral of its rate $\dot{p}_{\mathrm{I}}$, following from the purely deviatoric plastic strain rate tensor $\dot{\boldsymbol{\varepsilon}}^{\mathrm{p}}_{\mathrm{I}}$ as

$$\dot{p}_{\mathrm{I}} = \sqrt{\frac{2}{3} \dot{\boldsymbol{\varepsilon}}^{\mathrm{p}}_{\mathrm{I}} : \dot{\boldsymbol{\varepsilon}}^{\mathrm{p}}_{\mathrm{I}}} \,. \tag{64}$$

The purely deviatoric plastic flow, as the time integral of $\dot{\boldsymbol{\varepsilon}}^{\mathrm{p}}_{\mathrm{I}}$ over the current reloading increment Eq. (60) and expressed as

$$\Delta\boldsymbol{\varepsilon}^{\mathrm{p}}_{\mathrm{I}} = \Delta p_{\mathrm{I}} \boldsymbol{N}_{\mathrm{I}} \,, \tag{65}$$

provides the current stress state correction, pointing back from the elastic trial reloading stress $\Delta\boldsymbol{\sigma}_{\mathrm{I}}^{\mathrm{re,tr}} = \mathbb{C}_{\mathrm{I}}^{\mathrm{el}} : \Delta\boldsymbol{\varepsilon}_{\mathrm{I}}^{\mathrm{re}}$ towards the actual reloading stress $\Delta\boldsymbol{\sigma}_{\mathrm{I}}^{\mathrm{re}}$. Therefore, the flow direction is given as

$$\boldsymbol{N}_{\mathrm{I}} = \frac{3}{2}\frac{\mathrm{dev}(\Delta\boldsymbol{\sigma}_{\mathrm{I}}^{\mathrm{re}})}{\Delta\sigma_{\mathrm{I}}^{\mathrm{re,eq}}} = \frac{3}{2}\frac{\mathrm{dev}(\Delta\boldsymbol{\sigma}_{\mathrm{I}}^{\mathrm{re,tr}})}{\Delta\sigma_{\mathrm{I}}^{\mathrm{re,tr,eq}}}\,, \tag{66}$$

and the stress state (Eq. (60b)) follows

$$\Delta\boldsymbol{\sigma}_{\mathrm{I}}^{\mathrm{re}} = \Delta\boldsymbol{\sigma}_{\mathrm{I}}^{\mathrm{re,tr}} - 2G_{\mathrm{I}}^{\mathrm{el}}\Delta p_{\mathrm{I}}\boldsymbol{N}_{\mathrm{I}}\,. \tag{67}$$

Following the elastic isotropy in Eq. (61), the incremental secant stiffness can be expressed as an isotropic tensor

$$\mathbb{C}_{\mathrm{I}}^{\mathrm{sec}} = 3\kappa_{\mathrm{I}}^{\mathrm{el}}\mathbb{I}^{\mathrm{vol}} + 2G_{\mathrm{I}}^{\mathrm{sec}}\mathbb{I}^{\mathrm{dev}}\,, \tag{68}$$

where the incremental shear modulus is given as

$$G_{\mathrm{I}}^{\mathrm{sec}} = \frac{\Delta\sigma_{\mathrm{I}}^{\mathrm{re,eq}}}{3\,\Delta\varepsilon_{\mathrm{I}}^{\mathrm{re,eq}}} = G_{\mathrm{I}}^{\mathrm{el}} - \frac{3(G_{\mathrm{I}}^{\mathrm{el}})^2\Delta p_{\mathrm{I}}}{\Delta\sigma_{\mathrm{I}}^{\mathrm{re,tr,eq}}}\,. \tag{69}$$

3. Multiscale modeling of the woven composite

The macroscopic response of the woven unit cell is predicted by a mesoscopic model order reduction, achieved through a spatial subdivision, and the use of either the TFA or the HS algorithm (Section 2.1.3). These reduced order models rely on an underlying spatial decomposition and numerically determined interaction tensors inside the actual composite material, and are therefore reasonable approaches for the modeling of complex structures, as the woven geometry. The homogenized mesoscopic response of the yarns, consisting of randomly distributed elastic fibers, occupying a volume fraction of 80 %, inside an elasto-plastic matrix material, is achieved using the MFH (Section 2.2).

3.1. Boundary conditions for the woven composite unit cell

Periodic boundary conditions (PBC) are typically applied for the modeling of material RVEs or unit cells. However, fully applied PBCs on all surfaces of the unit cell may provide mechanical responses that deviate strongly from experimental results on laminates of woven composites. It was shown that simulation results using modified PBCs, where the surfaces with the ouf-of-plane normals (normals in vertical χ_3-direction) are kept flat without any distortion (without a fixation of the vertical motion of the faces), deliver results that mirror the experimental results much more closely (Wu et al., 2021a). The modified PBCs are referred to as mixed boundary conditions (MBC). The better results of using the MBC are explained by the fact that the use of flat upper and lower ply surfaces corresponds more accurately to the actual deformation modes of a woven composite laminate. The MBC are applied for all loading cases in the offline stage and during the non-linear analyses of the woven composite.

3.2. Offline stage: mesostructure and mesomechanics based model order reduction

The model order reduction step consists of a spatial division of the fully discretized material domain, in this work the mesoscale woven composite unit cell, into several subdomains. An optimized subdomain decomposition is achieved using the k-means clustering technique. The k-means clustering partitions a number of local data points into subpartitions based on the similarity of the local data. The final partition is achieved by solving an optimization problem iteratively, minimizing the deviations between all local data points and the subpartition mean values. In the context of mechanical fields, the k-means clustering divides the considered domain based on the similarity of the local mechanical behavior.

As shown by Spilker et al. (2022), respecting inelastic deformation patterns within a material allows an improved subdomain decomposition in comparison to the decomposition based on purely elastic deformation. In this work, the three inelastic deformation boundary modes

$$\overline{\boldsymbol{\varepsilon}}^{\mathrm{in}(1)} = E^{\mathrm{in}}(\vec{e}_1 \otimes \vec{e}_1 - \vec{e}_2 \otimes \vec{e}_2) \tag{70a}$$

$$\overline{\boldsymbol{\varepsilon}}^{\mathrm{in}(2)} = E^{\mathrm{in}}(\vec{e}_2 \otimes \vec{e}_2 - \vec{e}_1 \otimes \vec{e}_1) \tag{70b}$$

$$\overline{\boldsymbol{\varepsilon}}^{\mathrm{in}(3)} = E^{\mathrm{in}}(\vec{e}_1 \otimes \vec{e}_2 + \vec{e}_2 \otimes \vec{e}_1)\,, \tag{70c}$$

with the overall deformation factor $E^{\mathrm{in}} = 3\%$ and the canonical unit vectors $\vec{e}_1$, $\vec{e}_2$, $\vec{e}_3$ in the 3D reference coordinate system χ_1, χ_2, χ_3, were selected and applied on the woven composite unit cell. The three chosen deformation modes inside the ply plane (χ_1–χ_2-plane) represent typical deformation conditions for the woven composite structure. The mesoscopic eigenstrain fields $\boldsymbol{\varepsilon}^{*(l)}(\boldsymbol{\chi})$ emerging under each of the boundary conditions $l = 1, 2, 3$ are computed.

Performed in this work is the clustering of the homogenized yarns of a mesoscopic unit cell. To accomplish a physically reasonable spatial division of a material with an underlying non-uniform microstructure into subdomains on the mesoscale, it is necessary to account for the microstructural distribution. In the particular case of the woven composite unit cell, the yarns have locally different orientations, leading to locally varying material properties and mechanical responses. However, the yarns are divided into subdomains which, in the solution stage of the clustering based ROMs, are considered to possess uniform effective fiber orientations and thus uniform elastic and inelastic material properties. As will be presented in Section 4.1, for good piecewise uniform approximations of the woven unit cell on the mesoscale, it is not sufficient to consider only mesoscopic mechanical fields for the spatial decomposition. An effective fiber orientation of a subdomain, computed as the homogenized fiber orientation of the mesoscopic material points contained in the subdomain, implies that mesoscopic material points with very deviating fiber orientations gathered in the same subdomain would lead to ill-representative effective fiber orientations of the subdomain. The result would be unreliable elastic and inelastic mechanical responses of the subdomain computed by the MFH algorithm. Therefore, the division of the mesoscopic yarns based on the microstructural yarn/fiber orientation (Han et al., 2020) is the necessary condition for valid responses of the yarns and of the unit cell. Consequently, additionally to the

mesoscopic inelastic strain distributions under the loading modes in Eq. (70), the local yarn/fiber orientation needs to be taken into account for the mesoscale spatial division. Therefore, in this work, each yarn domain V_Y ($Y = \text{Weft}, \text{Warp}$) is spatially divided in two steps:

1. First, the necessary division based on the fiber orientation at the mesoscopic material points (described in Section 2.2.1) is performed. Each yarn domain V_Y is decomposed into K_Y^θ subdomains V_R, $R \in 1, ..., K_Y^\theta$. A sufficiently high K_Y^θ ensures that only mesoscopic material points with similar fiber orientation are gathered in one subdomain and therefore reasonable homogenized fiber orientations of the subdomain. For a general orientation-based subdivision, the function

$$J_Y^\theta[\theta(\boldsymbol{\chi})] = \sum_{R=1}^{K_Y^\theta} \sum_{i=1}^{N_R} |\vec{v}(\boldsymbol{\chi}_i) \times \vec{v}_R|^2, \quad \boldsymbol{\chi} \in V_Y, \quad \boldsymbol{\chi}_i \in V_R \subset V_Y, \quad R \in 1, ..., K_Y^\theta, \tag{71}$$

   can be chosen to be minimized, where N_R is the number of mesoscopic material points inside the subdomain R, $\vec{v}(\boldsymbol{\chi}_i)$ and $\vec{v}_R$ are the local and subdomain fiber orientations given by Eqs. (35) and (39). The operation " $\times$ " denotes the cross product between two vectors $\vec{a}$ and $\vec{b}$, defined as

$$\vec{a} \times \vec{b} = |a|\,|b|\,\sin(\Delta\theta)\,, \tag{72}$$

   where $\Delta\theta$ is the angle between the two vectors in the plane they are located in. The cross product between the local fiber orientation $\vec{v}(\boldsymbol{\chi}_i)$ and the subdomain mean orientation $\vec{v}_R$ in above Eq. (71) represents the deviation of $\vec{v}(\boldsymbol{\chi}_i)$ from $\vec{v}_R$. In the case of the woven structure, the first euler rotation is uniform per yarn, meaning that all local fiber orientations in one yarn are distinguished only by the second euler angle $\theta_2(\boldsymbol{\chi})$. Since each yarn is subdivided separately, and considering Eq. (72), the k-means clustering is applied to minimize the simplified function

$$J_Y^\theta[\theta(\boldsymbol{\chi})] = \sum_{R=1}^{K_Y^\theta} \sum_{i=1}^{N_R} \big(\sin(\theta_2(\boldsymbol{\chi}_i) - \theta_{2_R})\big)^2, \quad \boldsymbol{\chi} \in V_Y, \quad \boldsymbol{\chi}_i \in V_R \subset V_Y, \quad R \in 1, ..., K_Y^\theta, \tag{73}$$

   where the subdomain mean orientation θ_{2_R} follows Eq. (36). It is noted that in this spatial division step, the yarns are clustered purely based on the local yarn orientation. Since the yarns have equal/similar inclinations in more than one region along the yarns longitudinal direction, the subdivision may lead to subdomains that are non-coherent volumes.

2. As the second spatial division step, the subdomain decomposition of the mesoscopic unit cell domain can be optimized by taking into account the mechanical behavior of the mesoscopic material points. The mechanical behavior is accounted for by the computation of mesoscopic eigenstrain fields $\boldsymbol{\varepsilon}^{*(l)}(\boldsymbol{\chi})$ occurring under the applied inelastic boundary modes in Eq. (70). Each orientation-based subdomain V_R is divided

into a number K_Y^{p} subdomains V_r, $r \in 1, ..., K_Y^{\mathrm{p}}$ based on the inelastic strain distributions. For the inelasticity-based subdomain refinement, the eigenstrain fields $\boldsymbol{\varepsilon}^{*(l)}(\boldsymbol{\chi})$ under each of the boundary conditions $l = 1, 2, 3$ are normalized by the equivalent (scalar) per-phase averaged eigenstrain and arranged in local 6×1 vectors $\boldsymbol{q}^{(l)}(\boldsymbol{\chi})$. The normalized eigenstrain fields are then assembled in local 1×18 vectors

$$\boldsymbol{q}(\boldsymbol{\chi}) = \left(\left(\boldsymbol{q}^{(1)}(\boldsymbol{\chi})\right)^{\mathrm{T}}, \left(\boldsymbol{q}^{(2)}(\boldsymbol{\chi})\right)^{\mathrm{T}}, \left(\boldsymbol{q}^{(3)}(\boldsymbol{\chi})\right)^{\mathrm{T}} \right)^{\mathrm{T}}, \tag{74}$$

representing the entire set of the gathered mesoscopic eigenstrain field information. The k-means clustering technique is then applied on the eigenstrain field information in each orientation-based subdomain R, minimizing the corresponding function

$$J_R^{\mathrm{p}}[\boldsymbol{q}(\boldsymbol{\chi})] = \sum_{r=1}^{K_Y^{\mathrm{p}}} \sum_{i=1}^{N_r} |\boldsymbol{q}(\boldsymbol{\chi}_i) - \boldsymbol{q}_r|^2, \quad \boldsymbol{\chi} \in V_R, \quad \boldsymbol{\chi}_i \in V_r \subset V_R \subset V_Y, \quad r \in 1, ..., K_Y^{\mathrm{p}}, \quad R \in 1, ..., K_Y^{\theta}, \tag{75}$$

where

$$|\boldsymbol{z}| = \sqrt{\boldsymbol{z} \cdot \boldsymbol{z}} \tag{76}$$

and the subdomain means $\boldsymbol{q}_r = \left(\left(\boldsymbol{q}_r^{(1)}\right)^{\mathrm{T}}, \left(\boldsymbol{q}_r^{(2)}\right)^{\mathrm{T}}, \left(\boldsymbol{q}_r^{(3)}\right)^{\mathrm{T}} \right)^{\mathrm{T}}$ follow from Eq. (26).

After both subdivision steps, the total number of subdomains per yarn is $K_Y = K_Y^{\mathrm{p}} K_Y^{\theta}$. It is noted that the isotropic matrix phase (subscript "I") is divided into a number K_{I} based on the local eigenstrain field distribution only. The total number of subdomains is therefore $K = K_{\mathrm{I}} + K_{\mathrm{Warp}} + K_{\mathrm{Weft}}$.

3.3. Transformation Field Analysis

After the division of all local points inside the mesoscopic unit cell domain into subdomains based inelastic fields and the local yarn orientation, the strain concentration tensors $\mathbb{A}_r^{\mathrm{el}}$ of the subdomains V_r are determined. The local elastic strain concentration tensor field $\mathbb{A}^{\mathrm{el}}(\boldsymbol{\chi})$ can be fully characterized by the computation of purely elastic strain fields $\boldsymbol{\varepsilon}(\boldsymbol{\chi})$ under the application of six orthogonal boundary condition modes $\overline{\boldsymbol{\varepsilon}}$. The average strain concentration tensors $\mathbb{A}_r^{\mathrm{el}}$ are then calculated as the average over the corresponding subdomain using Eq. (26). The interaction tensors $\mathbb{D}_{rs}$, representing elastic influence factors of a uniform eigenstrain in the subdomain V_s on the average strain in the subdomain V_r, are characterized by applying six orthogonal uniform eigenstrain modes $\boldsymbol{\varepsilon}_s^*$ in each subdomain V_s one by one in the purely elastic unit cell under a vanishing overall strain $\overline{\boldsymbol{\varepsilon}} = 0$ (Eq. (21)), and the computation of the average reaction strain field $\boldsymbol{\varepsilon}_r$ in every subdomain V_r.

After both the subdomain strain concentration tensors for and the interaction tensors between all subdomains are computed, the TFA formulation

$$\Delta\boldsymbol{\varepsilon}_r - \mathbb{A}_r^{\mathrm{el}} : \Delta\overline{\boldsymbol{\varepsilon}} - \sum_{s=1}^{K} \mathbb{D}_{rs} : \Delta\boldsymbol{\varepsilon}_s^* = 0\,, \tag{77}$$

can be solved incrementally. Details on the offline and online solution stages are given by Spilker et al. (2022).

3.4. Hashin-Shtrikman type approach

As an alternative approach to the TFA, the HS type analysis is deployed for the prediction of the response of nonlinear composites. The reduced incremental HS scale coupling relation (Eq. (32)) is recalled:

$$\Delta\boldsymbol{\varepsilon}_r = \Delta\overline{\boldsymbol{\varepsilon}} + \sum_{s=1}^{K} \Gamma_{rs} : \left(\Delta\boldsymbol{\sigma}_s - \mathbb{C}^{\mathrm{iso}} : \Delta\boldsymbol{\varepsilon}_s\right), \tag{78}$$

relying on the isotropic stiffness operator $\mathbb{C}^{\mathrm{iso}}$ of the reference medium and the Green's interaction tensors in the reference medium

$$\Gamma_{rs} = f\left((\mathbb{C}^{\mathrm{iso}})^{-1}\right) \propto (\mathbb{C}^{\mathrm{iso}})^{-1}. \tag{79}$$

Details on the construction of the HS type analysis in Eq. (78) will be given subsequently. The definition of the nonlinear reference medium with the stiffness $\mathbb{C}^{\mathrm{iso}}$, accounting for nonlinear homogenized responses, and the determination of the Green's tensors Γ_{rs} in the nonlinear medium, will be presented.

3.4.1. Numerical determination of the Green's tensors in the elastic medium

The homogenized elastic stiffness $\overline{\mathbb{C}}^{\mathrm{el}}$ of the material body V is, following Eq. (20), computed as

$$\overline{\mathbb{C}}^{\mathrm{el}} = \frac{1}{|V|}\int_V \mathbb{C}^{\mathrm{el}}(\boldsymbol{\chi}) : \mathbb{A}^{\mathrm{el}}(\boldsymbol{\chi})\mathrm{d}\boldsymbol{\chi}. \tag{80}$$

The approach proposed by Moakher and Norris (2006), yielding the closest isotropic stiffness tensor to an anisotropic one based on the minimal Euclidean distance, is used to determine the isotropic elastic reference stiffness

$$\mathbb{C}^{0,\mathrm{iso}} = 3\,\kappa^0\,\mathbb{I}^{\mathrm{vol}} + 2\,G^0\,\mathbb{I}^{\mathrm{dev}}. \tag{81}$$

The equivalent homogenized bulk modulus κ^0 and shear modulus G^0 are determined as

$$\kappa^0 = \frac{1}{3}\,\mathrm{Tr}(\overline{\mathbb{C}}^{\mathrm{el}} : \mathbb{I}^{\mathrm{vol}}) \tag{82}$$

and

$$G^0 = \frac{1}{10}\,\mathrm{Tr}(\overline{\mathbb{C}}^{\mathrm{el}} : \mathbb{I}^{\mathrm{dev}}), \tag{83}$$

where the trace of a fourth order tensor is computed as

$$\mathrm{Tr}(\mathbb{Z}) = \mathbb{Z}_{ijij} \tag{84}$$

using the Einstein convention.

The influence function $\Gamma^0(\boldsymbol{\chi}, \boldsymbol{\chi}')$ is computed inside the homogeneous medium with the isotropic stiffness $\mathbb{C}^{0,\mathrm{iso}}$. In a domain with the homogeneous stiffness $\mathbb{C}^{0,\mathrm{iso}}$, the polarization stress field $\boldsymbol{\tau}(\boldsymbol{\chi})$ in Eq. (10) equals the externally applied eigenstress field $\boldsymbol{\sigma}^*(\boldsymbol{\chi})$. With a

vanishing overall strain $\overline{\boldsymbol{\varepsilon}} = 0$, and a uniform eigenstress $\boldsymbol{\sigma}_s^*$ inside one subdomain V_s, the average strain in a subdomain V_r is given as

$$\boldsymbol{\varepsilon}_r = \Gamma_{rs}^0 : \boldsymbol{\sigma}_s^* . \tag{85}$$

The influence tensors between the subdomains,

$$\Gamma_{rs}^0 \propto (\mathbb{C}^{0,\mathrm{iso}})^{-1} , \tag{86}$$

can be fully characterized by applying the uniform eigenstress modes

$$\boldsymbol{\sigma}^*(\boldsymbol{\chi}') = \boldsymbol{\sigma}_s^*, \; \boldsymbol{\chi}' \in V_s , \quad s = 1, ...K \tag{87}$$

in each subdomain V_s one at a time, simultaneously to the fixed zero overall strain $\overline{\boldsymbol{\varepsilon}} = 0$, and computing the average strain in the subdomain V_r. The eigenstrain modes in 3D analyses are

$$\boldsymbol{\sigma}_s^{*(1)} = S^* \vec{e}_1 \otimes \vec{e}_1 \tag{88a}$$
$$\boldsymbol{\sigma}_s^{*(2)} = S^* \vec{e}_2 \otimes \vec{e}_2 \tag{88b}$$
$$\boldsymbol{\sigma}_s^{*(3)} = S^* \vec{e}_3 \otimes \vec{e}_3 \tag{88c}$$
$$\boldsymbol{\sigma}_s^{*(4)} = \frac{1}{2} S^* (\vec{e}_1 \otimes \vec{e}_2 + \vec{e}_2 \otimes \vec{e}_1) \tag{88d}$$
$$\boldsymbol{\sigma}_s^{*(5)} = \frac{1}{2} S^* (\vec{e}_1 \otimes \vec{e}_3 + \vec{e}_3 \otimes \vec{e}_1) \tag{88e}$$
$$\boldsymbol{\sigma}_s^{*(6)} = \frac{1}{2} S^* (\vec{e}_2 \otimes \vec{e}_3 + \vec{e}_3 \otimes \vec{e}_2), \tag{88f}$$

with the eigenstress factor S^*.

3.4.2. Adaptation of the reference stiffness and the Green's operator

The isotropic reference stiffness of the material $\mathbb{C}^{\mathrm{iso}}$ in Eq. (14),

$$\mathbb{C}^{\mathrm{iso}} = 3\,\kappa\,\mathbb{I}^{\mathrm{vol}} + 2\,G\,\mathbb{I}^{\mathrm{dev}} , \tag{89}$$

can as well be formulated as a function of the shear modulus G and the Poisson ratio

$$\nu = \frac{3\,\kappa - 2\,G}{2\,(3\,\kappa + G)} \tag{90}$$

of the reference medium, such that

$$\begin{aligned} \mathbb{C}^{\mathrm{iso}}_{kkkk} &= 2\,G \frac{1-\nu}{1-2\,\nu} \\ \mathbb{C}^{\mathrm{iso}}_{jjkk} &= 2\,G \frac{\nu}{1-2\,\nu} \\ \mathbb{C}^{\mathrm{iso}}_{jkjk} &= G , \end{aligned} \tag{91}$$

Algorithm 1: Numerical incremental HS type analysis procedure using the tangent shear modulus $\overline{G}^{\mathbf{tan}}$ at a glance: Newton-Raphson scheme at one load step for a given overall strain increment $\Delta\overline{\boldsymbol{\varepsilon}}$.

initialize: $\Delta\boldsymbol{\varepsilon}_r = \Delta\overline{\boldsymbol{\varepsilon}}$ $(r = 1, ..., K)$
iterative procedure:
repeat
  for $r = 1, K$ **do**
    call constitutive relations for subdomain V_r to compute $\boldsymbol{\sigma}_r$ and $\mathbb{C}_r^{\text{alg}}$ from the MFH unloading-reloading procedure in Section 2.2.3 for the yarns and following Section 2.3 for the matrix phase
  end
  compute $\Delta\overline{\sigma}^{\text{eq}}$, $\Delta\overline{\varepsilon}^{\text{eq}}$ from the incremental stress $\Delta\overline{\boldsymbol{\sigma}}$ and strain $\Delta\overline{\boldsymbol{\varepsilon}}$ with Eq. (62) and $G = \overline{G}^{\mathbf{tan}}$ following Eq. (98)
  for $r = 1, K$ **do**
    initialize residual $\boldsymbol{F}_r = \Delta\boldsymbol{\varepsilon}_r - \Delta\overline{\boldsymbol{\varepsilon}}$
    for $s = 1, K$ **do**
      add polarization influence contribution to residual: $\boldsymbol{F}_r = \boldsymbol{F}_r - \Gamma^0_{rs} : \left[(G^0/G)\,\Delta\boldsymbol{\sigma}_s - \mathbb{C}^0 : \Delta\boldsymbol{\varepsilon}_s\right]$
      compute Jacobian matrix $\mathbb{J}_{rs}$ (Eq. (103))
    end
  end
  solve $\delta[\boldsymbol{\varepsilon}] = \{\mathbb{J}\}^{-1} : [\boldsymbol{F}]$
  update $[\Delta\boldsymbol{\varepsilon}] = [\Delta\boldsymbol{\varepsilon}] - \delta[\boldsymbol{\varepsilon}]$
until $|[\boldsymbol{F}]| <$ tol;
after convergence:
compute $\overline{\boldsymbol{\sigma}}$ and $\overline{\mathbb{C}}^{\text{alg}}$, following Eq. (109) and Eq. (112), respectively.

with no sum on k or j intended. Following Eq. (91), the stiffness of the elastic reference medium $\mathbb{C}^{0,\text{iso}}$ has the entries

$$\begin{aligned} \mathbb{C}^{0,\text{iso}}_{kkkk} &= 2\,G^0\,\frac{1-\nu^0}{1-2\,\nu^0} \\ \mathbb{C}^{0,\text{iso}}_{jjkk} &= 2\,G^0\,\frac{\nu^0}{1-2\,\nu^0} \\ \mathbb{C}^{0,\text{iso}}_{jkjk} &= G^0\,, \end{aligned} \tag{92}$$

with the shear modulus G^0 and the Poisson ratio ν^0 of the elastic reference medium.

For an accurate modeling of the nonlinear responses of composite materials, the reference medium needs to be adapted to the instantaneous response of the composite (Liu et al., 2016; Wulfinghoff et al., 2018). Wulfinghoff et al. (2018) suggested the assumption of a constant Poisson ratio of the nonlinear reference medium

$$\nu = \nu^0\,, \tag{93}$$

such that

$$\mathbb{C}^{\text{iso}}(G,\nu) \rightarrow \mathbb{C}^{\text{iso}}(G)\,. \tag{94}$$

Following the expressions Eqs. (91) and (92), and with the (non-physical) assumption of a constant Poisson ratio of the reference medium during inelastic deformation (Eq. (93)), the current isotropic reference stiffness $\mathbb{C}^{\text{iso}}$ and the influence tensors Γ_{rs} during inelastic deformation of the material can be achieved solely by an adaption of the instantaneous reference shear modulus G:

$$\mathbb{C}^{\text{iso}}(G) = \frac{G}{G^0}\,\mathbb{C}^{0,\text{iso}}\,, \tag{95}$$

and

$$\Gamma_{rs} = \Gamma^0_{rs} : \mathbb{C}^{0,\text{iso}} : (\mathbb{C}^{\text{iso}})^{-1} = \frac{G^0}{G}\,\Gamma^0_{rs}\,. \tag{96}$$

3.4.3. Expression of the instantaneous shear modulus

As proposed by Wulfinghoff et al. (2018); Cavaliere et al. (2020), the reference shear modulus is computed as

$$G = \overline{G}^{\mathbf{sec}} = \frac{\overline{\sigma}^{\text{eq}}}{3\,\overline{\varepsilon}^{\text{eq}}}, \tag{97}$$

where $\overline{G}^{\mathbf{sec}}$ is the total secant shear modulus of the composite. The equivalent homogenized strain $\overline{\varepsilon}^{\text{eq}}$ and stress $\overline{\sigma}^{\text{eq}}$ are computed from $\overline{\boldsymbol{\varepsilon}}$ and $\overline{\boldsymbol{\sigma}}$, respectively, with Eq. (62). The use of the total secant shear modulus Eq. (97) has two clear disadvantages:

- If the material is being elastically deformed after a previous inelastic loading history, as the case during an unloading stage, the physical instantaneous homogenized stiffness of the composite material equals the elastic stiffness of the composite. However, the isotropic reference stiffness and the Green's tensors do not equal the elastic isotropized stiffness of the material.

- During unloading stages after previous inelastic deformation, the states of a total equivalent strain $\overline{\varepsilon}^{\text{eq}} = 0$ or stress $\overline{\sigma}^{\text{eq}} = 0$ (e.g., in a uniaxial stress test) can occur in the material. These cases imply singularities of the reference stiffness or of the Green's operators in the vicinity of these points, prohibiting reasonable predictions for the mechanical response of the composite material.

For this sake, the reference shear modulus in this paper is computed as the incrementally computed secant shear modulus of the material

$$G = \overline{G}^{\mathbf{tan}} = \frac{\Delta\overline{\sigma}^{\text{eq}}}{3\,\Delta\overline{\varepsilon}^{\text{eq}}}\,, \tag{98}$$

with the incremental equivalent homogenized stresses and strains, following from $\Delta\overline{\boldsymbol{\varepsilon}}$ and $\Delta\overline{\boldsymbol{\sigma}}$ with Eq. (62). Since this incremental secant formulation represents an approximated tangential shear modulus, the instantaneous shear modulus is denoted as $\overline{G}^{\mathbf{tan}}$. In contrast to the secant formulation in Eq. (97), the elastic response of the reference material during instantaneous elastic loading is recovered, unaffected by any previous inelastic loading history.

3.4.4. Solution procedure using the HS algorithm

In the following, the equations required to solve a mechanical problem using the HS analysis algorithm are derived. A schematic overview of the numerical HS solution procedure is demonstrated in Algorithm 1. The incremental HS analysis algorithm is expressed by Eq. (78). Considering the two Eqs. (95) and (96), the HS algorithm in Eq. (78) can as well be formulated as

$$\begin{aligned}\Delta\boldsymbol{\varepsilon}_r &= \Delta\overline{\boldsymbol{\varepsilon}} + \sum_{s=1}^{K} \frac{G^0}{G}\Gamma^0_{rs} : \left(\Delta\boldsymbol{\sigma}_s - \frac{G}{G^0}\mathbb{C}^{0,\mathrm{iso}} : \Delta\boldsymbol{\varepsilon}_s\right) \\ &= \Delta\overline{\boldsymbol{\varepsilon}} + \sum_{s=1}^{K} \Gamma^0_{rs} : \left(\frac{G^0}{G}\Delta\boldsymbol{\sigma}_s - \mathbb{C}^{0,\mathrm{iso}} : \Delta\boldsymbol{\varepsilon}_s\right),\end{aligned} \tag{99}$$

where the instantaneous shear modulus G is computed as presented in Eq. (98). The numerical solution of this system under a prescribed overall strain $\bar{\boldsymbol{\varepsilon}}$ is found using a Newton-Raphson procedure with the subdomain residuals

$$\boldsymbol{F}_r = \Delta\boldsymbol{\varepsilon}_r - \Delta\overline{\boldsymbol{\varepsilon}} - \sum_{s=1}^{K} \Gamma^0_{rs} : \left(\frac{G^0}{G}\Delta\boldsymbol{\sigma}_s - \mathbb{C}^{0,\mathrm{iso}} : \Delta\boldsymbol{\varepsilon}_s\right), \tag{100}$$

iteratively solving the problem $\boldsymbol{F}_r = 0$ by the linearization

$$\boldsymbol{F}_r \to \boldsymbol{F}_r + \delta\boldsymbol{F}_r = 0. \tag{101}$$

Expressed as an assembled system using the $K \times 1$ block column vectors denoted by "[ ]" and the square $K \times K$ block matrices denoted by "{ }", the variational term $\delta[\boldsymbol{F}]$ follows as

$$\delta[\boldsymbol{F}] = \left\{\frac{\partial\boldsymbol{F}}{\partial\boldsymbol{\varepsilon}}\right\} : \delta[\boldsymbol{\varepsilon}] + \frac{\partial[\boldsymbol{F}]}{\partial\overline{\boldsymbol{\varepsilon}}} : \delta\overline{\boldsymbol{\varepsilon}} = \{\mathbb{J}\} : \delta[\boldsymbol{\varepsilon}] + \frac{\partial[\boldsymbol{F}]}{\partial\overline{\boldsymbol{\varepsilon}}} : \delta\overline{\boldsymbol{\varepsilon}}\,. \tag{102}$$

The full Jacobian system $\{\mathbb{J}\}$ consists of the single matrices (no sum on s intended)

$$\mathbb{J}_{rs} = \frac{\partial\boldsymbol{F}_r}{\partial\boldsymbol{\varepsilon}_s} = \delta_{rs}\mathbb{I} - \Gamma^0_{rs} : \left(\frac{G^0}{G}\mathbb{C}^{\mathrm{alg}}_s - \mathbb{C}^{0,\mathrm{iso}}\right) + \frac{G^0}{G^2}\left[\sum_{p=1}^{K}\Gamma^0_{rp} : \Delta\boldsymbol{\sigma}_p\right] \otimes \frac{\partial G}{\partial\boldsymbol{\varepsilon}_s}\,, \tag{103}$$

with the instantaneous stiffness of the subdomains $\partial\Delta\boldsymbol{\sigma}_s/\partial\boldsymbol{\varepsilon}_s = \mathbb{C}^{\mathrm{alg}}_s$ (Eq. (59)). The derivative $\partial G/\partial\boldsymbol{\varepsilon}_s = \partial\overline{G}^{\mathbf{tan}}/\partial\boldsymbol{\varepsilon}_s$ is, following Eq. (98), computed as

$$\frac{\partial\overline{G}^{\mathbf{tan}}}{\partial\boldsymbol{\varepsilon}_s} = \frac{1}{3\,\Delta\overline{\varepsilon}^{\mathrm{eq}}}\frac{\partial\Delta\overline{\sigma}^{\mathrm{eq}}}{\partial\boldsymbol{\varepsilon}_s} - \frac{\Delta\overline{\sigma}^{\mathrm{eq}}}{3\,(\Delta\overline{\varepsilon}^{\mathrm{eq}})^2}\frac{\partial\Delta\overline{\varepsilon}^{\mathrm{eq}}}{\partial\boldsymbol{\varepsilon}_s} \tag{104}$$

with

$$\frac{\partial\Delta\overline{\sigma}^{\mathrm{eq}}}{\partial\boldsymbol{\varepsilon}_s} = \frac{3}{2}\upsilon_s\frac{\mathrm{dev}(\Delta\overline{\boldsymbol{\sigma}})}{\Delta\overline{\sigma}^{\mathrm{eq}}} : \mathbb{C}^{\mathrm{alg}}_s \tag{105}$$

and

$$\frac{\partial \Delta \overline{\varepsilon}^{\mathrm{eq}}}{\partial \boldsymbol{\varepsilon}_s} = \frac{2}{3} \upsilon_s \frac{\mathrm{dev}(\Delta \overline{\boldsymbol{\varepsilon}})}{\Delta \overline{\varepsilon}^{\mathrm{eq}}} \,. \tag{106}$$

Assuming a constant homogenized strain, implying $\delta \overline{\boldsymbol{\varepsilon}} = 0$, the result

$$\delta[\boldsymbol{\varepsilon}] = -\{\mathbb{J}\}^{-1} : [\boldsymbol{F}] \tag{107}$$

is used to correct the strain increments in the subdomains by

$$[\boldsymbol{\varepsilon}] = [\boldsymbol{\varepsilon}] + \delta[\boldsymbol{\varepsilon}] \tag{108}$$

per iteration. Once the computed strain increments of the subdomains have converged, the homogenized stress response is given by

$$\overline{\boldsymbol{\sigma}} = \sum_{r=1}^{K} \upsilon_r \boldsymbol{\sigma}_r \,. \tag{109}$$

The homogenized instantaneous stiffness is computed as

$$\overline{\mathbb{C}}^{\mathrm{alg}} = \frac{\partial \overline{\boldsymbol{\sigma}}}{\partial \overline{\boldsymbol{\varepsilon}}} = \sum_{r=1}^{K} \upsilon_r \frac{\partial \Delta \boldsymbol{\sigma}_r}{\partial \boldsymbol{\varepsilon}_r} \frac{\partial \boldsymbol{\varepsilon}_r}{\partial \overline{\boldsymbol{\varepsilon}}} \,, \tag{110}$$

where $\partial \Delta \boldsymbol{\sigma}_r / \partial \boldsymbol{\varepsilon}_r$ corresponds to the tangent operator of the subdomain (Eq. (59)). The second term $\partial \boldsymbol{\varepsilon}_r / \partial \overline{\boldsymbol{\varepsilon}}$, representing the subdomains instantaneous strain concentrations, follows after the solution in Eq. (102) as

$$\frac{\partial [\boldsymbol{\varepsilon}]}{\partial \overline{\boldsymbol{\varepsilon}}} = -\{\mathbb{J}\}^{-1} : \frac{\partial [\boldsymbol{F}]}{\partial \Delta \overline{\boldsymbol{\varepsilon}}} = \{\mathbb{J}\}^{-1} : [\mathbb{I}] \,. \tag{111}$$

The resulting full expression of Eq. (110) amounts to

$$\overline{\mathbb{C}}^{\mathrm{alg}} = \sum_{r=1}^{K} \upsilon_r \mathbb{C}_r^{\mathrm{alg}} : \left[\sum_{s=1}^{K} \{\mathbb{J}\}_{rs}^{-1} \right] . \tag{112}$$

4. Numerical Applications

The presented combined scale bridging techniques are used for nonlinear analyses of a woven composite unit cell (Fig. 4). The unit cell V geometry is the one used in Wu et al. (2021c), and is built following the methodology:

- The yarns cross-section is an ellipse of semi-axes a_0 and b_0;
- The size of the unit cell is $L \times L \times t$;

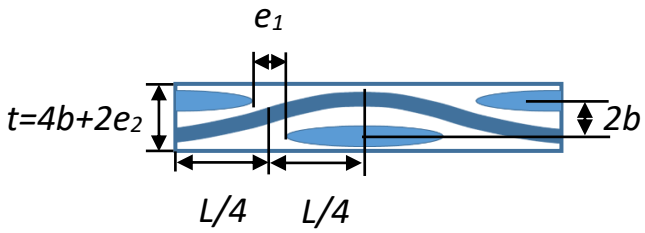

Figure 4: Cross-section geometry of the woven unit-cell following Wu et al. (2021c).

Table 1: Geometrical description of the woven unit cell.

Geometrical relationships	Value
Cell length $L = 4a_0 + 2e_1$ [mm]	3.294
Cell thickness $t = 4b + 2e_2$ [mm]	0.2245
Yarn axis location $b = \xi b_0$ [mm]	0.053625
Vertical distance between yarns $\alpha = 2\left(\frac{1}{1+\exp\left(-\frac{l\,L}{4}\right)} - \frac{1}{2}\right)$ [-]	0.99889
Yarn cross-section area A_0 [mm^2]	0.12
Yarn small semi-axis b_0 [mm]	0.04875
Yarn large semi-axis $a_0 = \frac{A_0}{\pi b_0}$ [mm]	0.78353
Yarns horizontal gap e_1 [mm]	0.08
Yarns vertical gap e_2 [mm]	0.005
Yarn eccentricity ξ [-]	1.1
Asymptoticy $l\,L$ [-]	30

- The central axis vertical location of a yarn along $\zeta = \chi_1$ or $\zeta = \chi_2$ reads

$$\chi_3 = b\left[\frac{2}{1+\exp\left(-\frac{l}{2}\left(2\zeta - \frac{L}{2}\right)\right)} - 1\right] \quad \text{for } \zeta \in [0;\, \frac{L}{2}]\,, \tag{113}$$

  where b governs the waviness of the yarn and l its asymptotic behaviour such that the yarn reaches the location αb with $\alpha = \frac{\chi_3\left(\frac{L}{2}\right)}{b}$;

- In order to avoid contact between yarns, the condition $b > b_0$ is enforced by constraining $b = \xi b_0$ with the eccentricity $\xi > 1$.

- The distances between the yarns in the cross-section is governed by e_1 and e_2, see Fig. 4;

The parameters are reported in Table 1. The total volume fraction of the yarns in the unit cell is 64.56 %. The yarns consist of the same matrix material, reinforced by fibers locally considered uni-directional (Fig. 2) with a orientation characterised by the Euler

Table 2: Material properties for the nonlinear analyses.

Matrix (M10.1 epoxy)		Fiber (UD300 HS(R) carbon fiber)	
Property	Value	Property	Value
Young's modulus E_{I} [GPa]	3.2	Young's modulus $E_{\mathrm{II}}^{\mathrm{L}}$ [GPa]	230
Poisson ratio ν_{I} [-]	0.3	Young's modulus $E_{\mathrm{II}}^{\mathrm{T}}$ [GPa]	40
Initial yield stress $\sigma_{\mathrm{I}}^{\mathrm{Y0}}$ [MPa]	30	Poisson ratio $\nu_{\mathrm{II}}^{\mathrm{TT}}$ [-]	0.2
Hardening modulus H_{I} [MPa] (offline)	130 (50)	Poisson ratio $\nu_{\mathrm{II}}^{\mathrm{LT}}$ [-]	0.256
Hardening exponent m_{I} [-]	300	Shear modulus $\mu_{\mathrm{II}}^{\mathrm{LT}}$ [GPa]	24

angle $76° \leq \theta_2(\boldsymbol{\chi}) \leq 104°$. In this work, the local volume fraction of the fiber material in the yarns is assumed uniform, and therefore: $\upsilon_{\mathrm{II}}(\boldsymbol{\chi}) = \upsilon_{\mathrm{II}} = 80\%$ and $\upsilon_{\mathrm{I}}(\boldsymbol{\chi}) = \upsilon_{\mathrm{I}} = 20\%$.

The mechanical properties of the isotropic elasto-plastic matrix material (index I) and of the transverse isotropic elastic fiber material (index II) are given in Table 2, where the longitudinal-transversal Poisson ratio of the elastic fibers is denoted as $\nu_{\mathrm{II}}^{\mathrm{LT}}$. The behavior of the matrix material is governed by the J_2-plasticity law with the hardening stress R_{I} following

$$R_{\mathrm{I}} = H_{\mathrm{I}} \left(1 - e^{-m_{\mathrm{I}}\, p_{\mathrm{I}}}\right), \tag{114}$$

where p_{I} is the equivalent accumulated plastic strain (Eq. (64)).

This section is divided into three parts: First, spatial subdivisions following the offline procedure described in Section 3.2 are displayed. The mesh for the DNS FE simulations, used for the offline stage and for comparison purpose, is built by 74146 linear tetrahedra. As the elements are linear, locking of the elements during elasto-plastic deformation is prevented by using the deformation gradient averaged over the element (de Souza Neto et al., 1996). Subsequently, elastic and inelastic responses of the woven composite unit cell during non-linear analyses, computed by the ROM techniques based on either TFA or HS, are investigated. The results achieved by the two ROM approaches are compared to each other and the results following the DNS for the same MBC (Section 3.1), which are also used throughout the offline stage. A discussion on the results then follows.

4.1. Effects of the spatial decomposition approaches

As described in Section 3.2, the spatial decomposition of the yarns of the woven composite unit cell has two contributions:

- The orientation based clustering, guaranteeing that only material points with similar local yarn/fiber orientations and thus mechanical responses are gathered in the same subdomain. The purely orientation based spatial decomposition of the yarns is displayed in Fig. 5.

- The consideration of inelastic fields for an improved account of the developing deformation patterns during inelastic loading conditions, shown to deliver improved results using the clustering based ROMs (Spilker et al., 2022; Spilker, 2022).

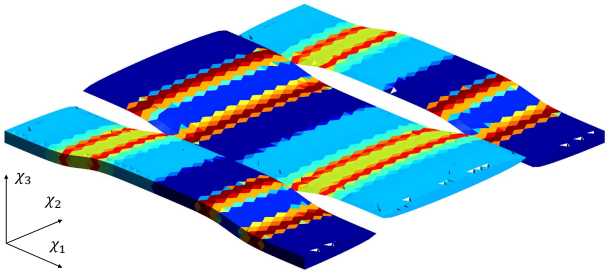

(a)

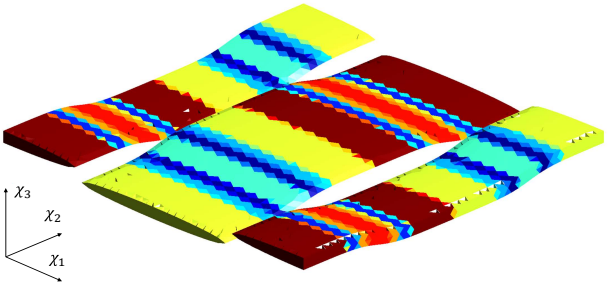

(b)

Figure 5: Spatial decompositions of the (a) weft yarn and (b) warp yarn of the mesoscale woven composite unit cell into eight subdomains each, solely based on the local yarn orientation.

The goal of the inelastic simulations conducted in the offline stage is the production of inelastic fields that exhibit detailed inelastic deformation patterns. This allows for an accurate capturing and representation of the essential features of inelastic deformation patterns by the spatial subdivision procedure using the k-means clustering technique. Lower hardening characteristics lead to more localized plasticity. More localized fields of inelastic deformation allow for an improved recognition of the inelastic deformation patterns, and in turn to improved inelasticity-based spatial divisions using the k-means clustering technique. For a better identification of the inelastic fields by the subdomains, the matrix hardening modulus in the offline stage DNS was reduced with respect to the real value, used during the actual non-linear analyses. It is noted that this manipulation of the inelastic material properties during the inelastic offline DNS has implications on the validity of the a-priori determined tensors neither for the TFA nor for the HS type analysis, all being evaluated from the elastic offline stage DNS only.

As visible when analysing the inelastic fields within the weft yarn (Figs. 6(a), 6(d) and 6(f)) and the warp yarn (Figs. 6(b), 6(e) and 6(g)), the inelastic deformation is represented by two major inelastic patterns:

- Transversally to the yarns main direction, localized in the regions of yarn inclination.
- Parallel to the yarns main direction, localized at the yarn edges.

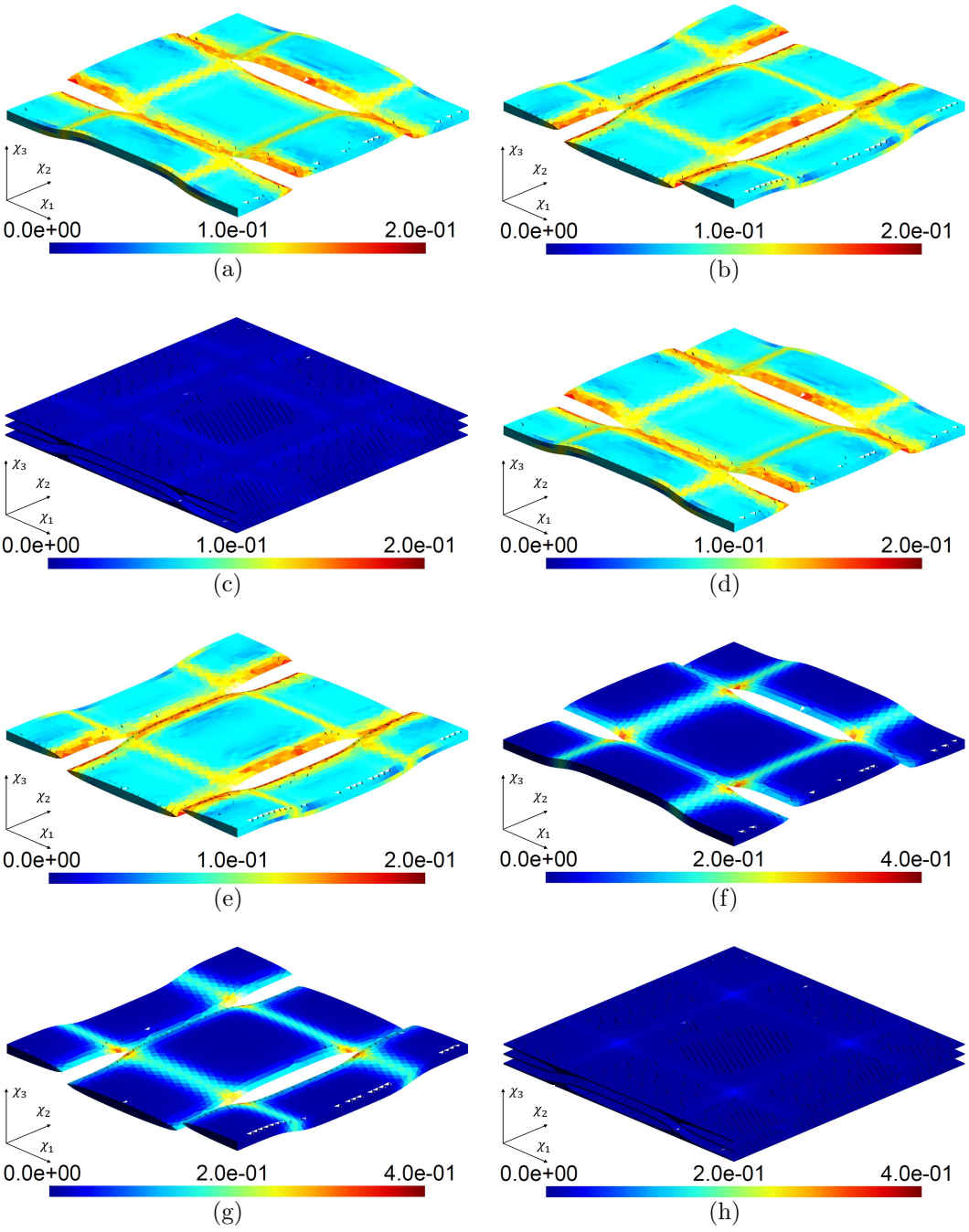

Figure 6: Equivalent plastic strain fields in the (a,d,f) weft and (b,e,g) warp yarns and the (c,h) pure matrix of the woven composite mesostructure during the application of the three inelastic boundary modes in the offline stage, (a,b,c) isochoric deformation with tension in χ_1-direction (weft yarn direction), (d,e) isochoric deformation with tension in χ_2-direction (warp yarn direction), (f,g,h) pure shearing in the ply-plane.

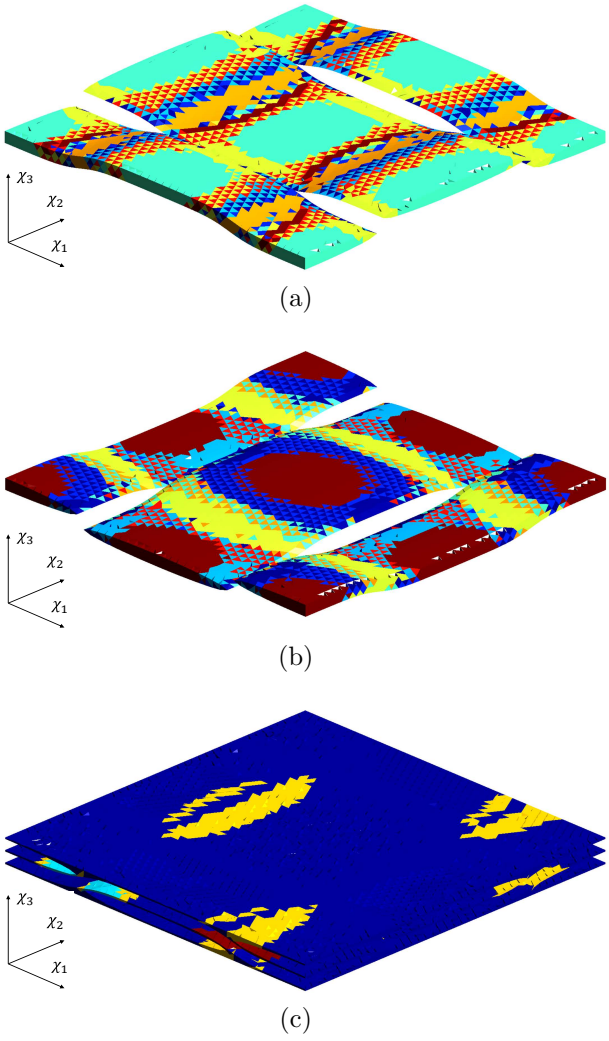

Figure 7: Spatial decompositions of the (a) weft yarn and (b) warp yarn of the mesoscale woven composite unit cell into eight subdomains each and of the (c) pure matrix phase into four subdomains, all based solely on eigenstrain tensor fields $\boldsymbol{\varepsilon}^{*(l)}(\boldsymbol{\chi})$ under the loading modes l in Eq. (70) (equivalent plastic strain fields are displayed in Fig. 6)

The resulting spatial decompositions of the yarns and the matrix purely based on the consideration of plastic strain fields are depicted in Fig. 7.

The inelastic deformation localized transversally to the yarns direction is accurately captured by the necessary spatial division step alone, taking into account the local yarn inclination. This can be recognized by a consideration of the purely orientation based decomposition, displayed in Figs. 5(a) and 5(b). The second major inelastic localization pattern, stretched out in the yarns main direction, is fully ignored by the clustering purely based on the yarns inclination. Therefore, the account for inelastic strains occurring during the application of the selected boundary modes provides adaptations of the spatial division,

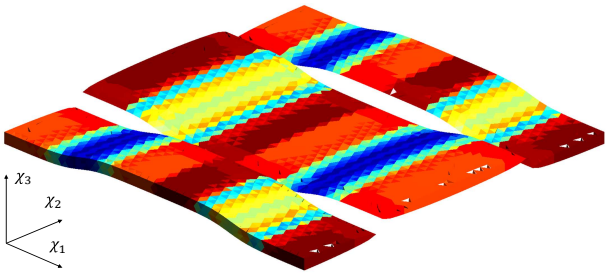

(a)

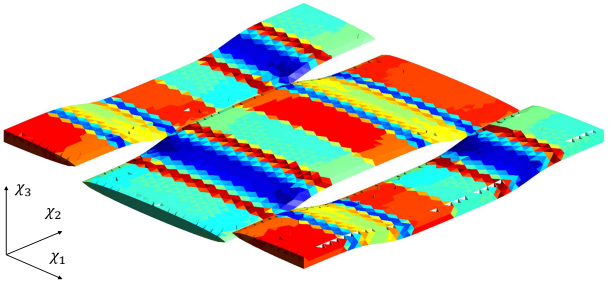

(b)

Figure 8: Spatial decompositions of the (a) weft yarn and (b) warp yarn of the mesoscale woven composite unit cell based on the local yarn orientation as the first division step, with refinements based on plastic strain fields.

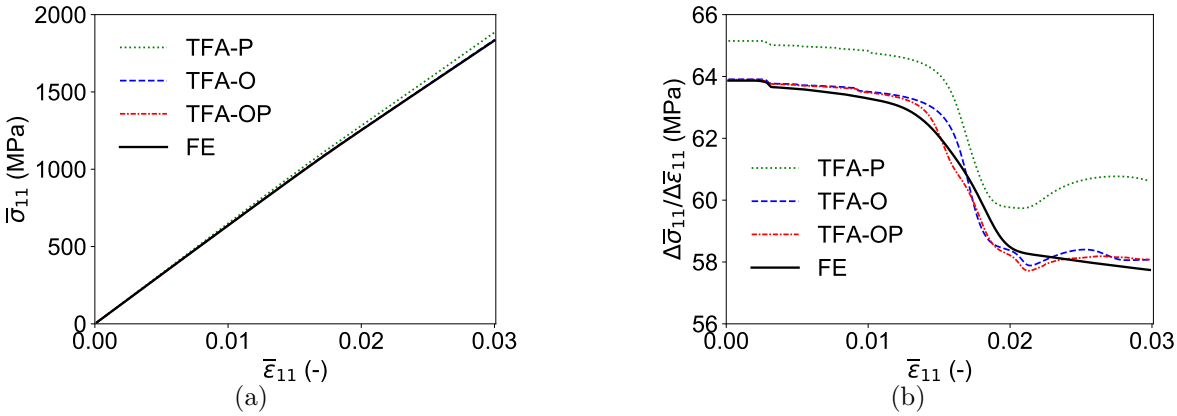

Figure 9: Computed homogenized (a) axial stress-strain response, (b) evolution of the incremental stress-strain ratio during a uniaxial tension test, with various underlying spatial decompositions: Purely based on the local yarn/fiber orientation (TFA-O, Fig. 5), purely based on plastic deformation fields (TFA-P, Fig. 7), and the division first based on the local orientation, refined in a second step by accounting for plastic fields (TFA-OP, Fig. 8).

refining the orientation-based subdomains by additionally respecting the inelastic patterns

in the yarns directions (Figs. 8(a) and 8(b)).

In the following, homogenized responses during a uniaxial tension test using the TFA with different underlying subdomain decompositions will be presented, allowing an evaluation of the effects of the various possible spatial decompositions. The matrix is always divided into $K_\mathrm{I} = 4$ subdomains based on plastic strain fields, as depicted in Fig. 7(c). The TFA relying on a decomposition of the yarns based on the yarn orientation alone will be referred to as TFA-O, the division based on mesoscopic plastic strains (eigenstrains) alone will be referred to as TFA-P, and the combined decomposition, consisting of a first orientation based clustering step and refinements based on plastic strain fields, as TFA-OP. The spatial decomposition is described as follows:

- TFA-O: A division of each yarn with $K_Y^\theta = 8$, $K_Y^\mathrm{p} = 1$. It means that each yarn is divided into $K_Y = K_Y^\theta = 8$ subdomains purely based on the local yarn/fiber orientation (Figs. 5(a) and 5(b)). In total, the unit cell is subdivided into $K = 20$ subdomains.
- TFA-P: A division of each yarn with $K_Y^\theta = 1$, $K_Y^\mathrm{p} = 8$. It means that each yarn is divided into $K_Y = K_Y^\theta = 8$ subdomains purely based on the plastic strain fields (Figs. 7(a) and 7(b)) under the offline loading modes. In total, the unit cell is subdivided into $K = 20$ subdomains.
- TFA-OP: A refinement of the orientation-based division into $K_Y^\theta = 8$ subdomains based on plastic deformation patterns with $K_Y^\mathrm{p} = 4$. Therefore, each yarn consists of $K_Y = 32$ subdomains after both spatial decomposition steps (Figs. 8(a) and 8(b)). The total subdomain number amounts to $K = 68$.

The results of the uniaxial tension test are presented in Fig. 9. It is visible that the TFA-P leads to too stiff results during elastic and inelastic deformation, while the TFA-O allows exact elastic and clearly improved inelastic predictions. The TFA-OP, due to the plastic field based refinements, leads to an improved capture of the yield onset, marked by the earlier drop of the incremental stress-strain ratio (Fig. 9(b)).

As already stated in Section 3.2, and proven above, the clustering based on the local yarn/fiber orientation is the necessary spatial decomposition step for woven composites. Consequently, only the purely orientation based and the combined spatial decompositions are used to produce the results in the following. The ROMs relying on a yarn subdivision purely based on the local orientation are referred to by the suffix "-O". Additionally to the orientation-based decomposition, the yarns subdomains were refined by means of the two-step clustering with a consideration of emerging inelastic fields ($K_Y^\mathrm{p} > 1$ in Section 3.2). The cases of a spatial division with an additional account of the inelastic deformation fields are referred to by the suffix "-OP".

4.2. Homogenized elastic behavior

The issue of a spatial decomposition of a material domain with non-uniform microstructural properties into subdomains with uniform effective microstructures and properties was treated in Section 3.2. Here, the prediction quality of the homogenized elastic behavior

Table 3: Elastic properties computed following Eqs. (115) and (116) using DNS and the TFA or HS algorithms.

method	DNS	TFA-O	TFA-P	TFA-OP	HS-O	HS-OP
$\overline{E}_1^{\mathrm{el}}$ (GPa)	63.9	63.9	65.5	63.9	64.6	64.6
$\overline{\nu}_{12}^{\mathrm{el}}$ (-)	4.11e-2	4.12e-2	4.45e-2	4.12e-2	4.10e-2	4.11e-2
$\overline{\nu}_{13}^{\mathrm{el}}$ (-)	4e-1	3.99e-1	3.41e-1	3.99e-1	3.85e-1	3.85e-1

of the woven unit cell modeled by the clustering based ROMs using uniform subdomains, relying on the different spatial decompositions in Section 4.1, is investigated. To this end, the elastic Young's modulus $\overline{E}_1^{\mathrm{el}}$ and the elastic Poisson ratios in the ply plane $\overline{\nu}_{12}^{\mathrm{el}}$ and out of the ply plane $\overline{\nu}_{13}^{\mathrm{el}}$ were identified as the instantaneous mechanical properties in the elastic regime as

$$\overline{E}_1^{\mathrm{el}} = \frac{\Delta\overline{\sigma}_{11}}{\Delta\overline{\varepsilon}_{11}} \quad \text{at } \overline{\varepsilon}_{11} = 0 \tag{115}$$

and

$$\overline{\nu}_{1j}^{\mathrm{el}} = \frac{\Delta\overline{\varepsilon}_{jj}}{\Delta\overline{\varepsilon}_{11}} \quad j = 2,3 \quad \text{at } \overline{\varepsilon}_{11} = 0\,. \tag{116}$$

All elastic properties are predicted almost exactly by the TFA-O and the TFA-OP, with deviations below 0.1 % from the elastic properties computed using DNS Table 3. The purely plasticity based spatial decomposition (TFA-P) leads to an overstiff prediction of the Young's modulus $\overline{E}_1^{\mathrm{el}}$, with an error of 2 %. The Poisson ratio is overestimated in the ply-plane ($\overline{\nu}_{12}^{\mathrm{el}}$) by 8 % and underestimated by 14 % out of the ply-plane ($\overline{\nu}_{13}^{\mathrm{el}}$).

The HS method provides good agreements of the elastic properties as well, however the error level is higher than the one achieved by the TFA. In particular, estimations slightly too stiff are provided for the longitudinal Young's modulus $\overline{E}_1^{\mathrm{el}}$.

4.3. Nonlinear analyses

Inelastic loading conditions $\overline{\boldsymbol{\varepsilon}}(t)$, $t = [0, T]$, $T = 1.0$ s, were applied on the woven composite unit cell, described by the following loading histories:

- Overall axial cyclic loading up to 6% strain in χ_1-axis orientation, see Fig. 10(a), with free motion in the orthogonal orientations, corresponding to overall uniaxial tension boundary conditions

$$\begin{aligned} &\overline{\varepsilon}_{11}(0) = 0 \rightarrow \overline{\varepsilon}_{11}(T/4) = 0.03 \rightarrow \overline{\varepsilon}_{11}(T/2) = -0.03 \\ &\qquad \rightarrow \overline{\varepsilon}_{11}(3T/4) = 0.06 \rightarrow \overline{\varepsilon}_{11}(T) = 0 \\ &\overline{\sigma}_{22} = \overline{\sigma}_{33} = 0 \end{aligned} \tag{117}$$

- Applied overall cyclic pure shearing loading up to 6%, see Fig. 10(a), with $\overline{\varepsilon}_{33} = \overline{\varepsilon}_{13} =$

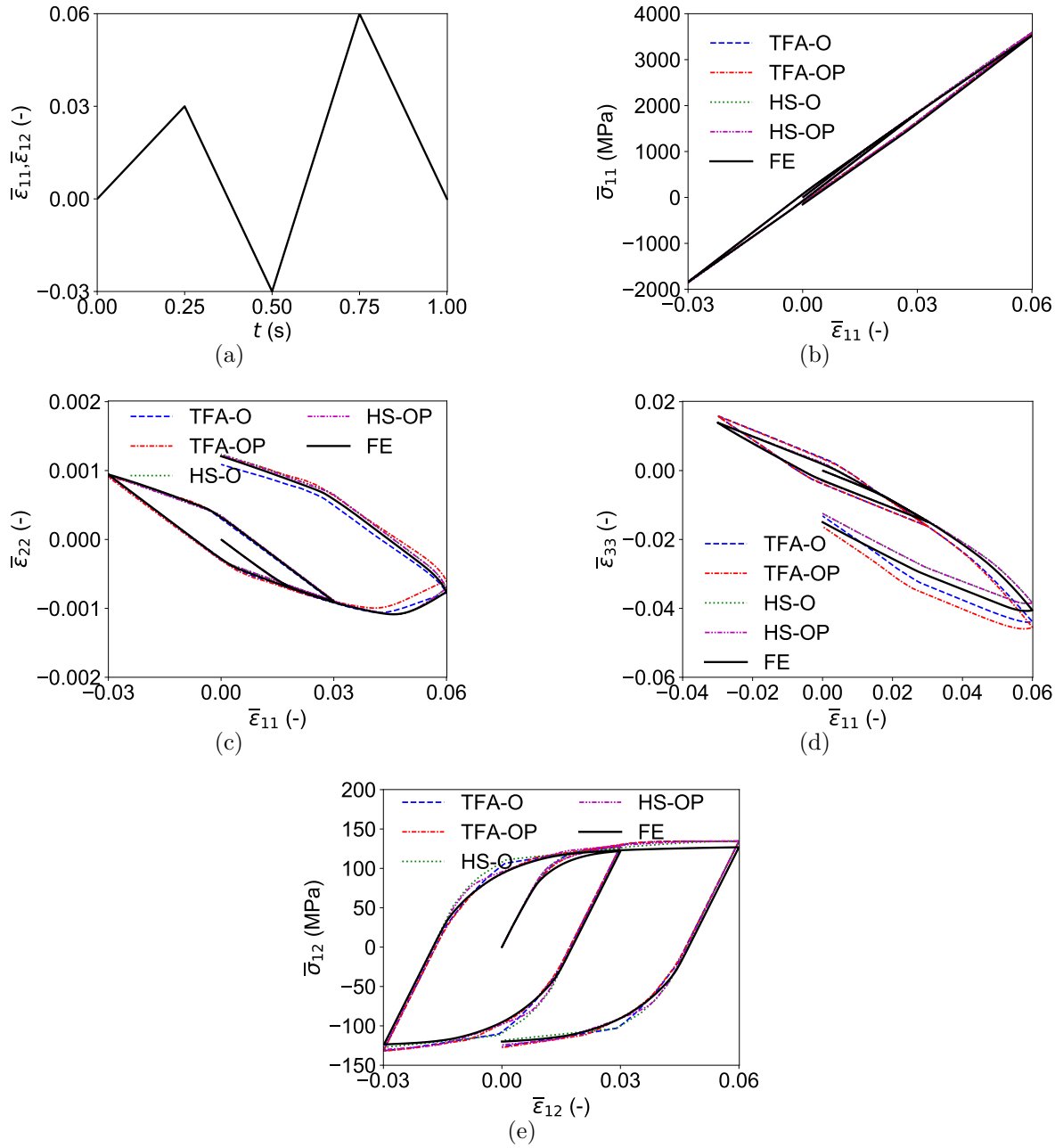

Figure 10: (a) Applied axial and shear deformation during the two separate uniaxial tension (Eq. (117)) and pure shear (Eq. (118)) tests. Uniaxial tension: evolution of the homogenized (b) axial stress and strain components perpendicular to the direction of tension (c) in plane and (d) out of plane. Pure-shear: evolution of the (e) homogenized shear stress.

$$\overline{\varepsilon}_{23} = 0\text{:}$$

$$\begin{aligned}\overline{\boldsymbol{\varepsilon}}(0) = \begin{pmatrix} 0 & 0 \\ 0 & 0 \end{pmatrix} \rightarrow \overline{\boldsymbol{\varepsilon}}(T/4) = \begin{pmatrix} 0.03 & 0 \\ 0 & 0.03 \end{pmatrix} \rightarrow \overline{\boldsymbol{\varepsilon}}(T/2) = \begin{pmatrix} -0.03 & 0 \\ 0 & -0.03 \end{pmatrix} \\ \rightarrow \overline{\boldsymbol{\varepsilon}}(3T/4) = \begin{pmatrix} 0 & 0.06 \\ 0.06 & 0 \end{pmatrix} \rightarrow \overline{\boldsymbol{\varepsilon}}(T) = \begin{pmatrix} 0 & 0 \\ 0 & 0 \end{pmatrix}.\end{aligned} \tag{118}$$

- Non-proportional loading, consisting of three different stages of uniaxial and shear deformation and a stage of simultaneous unloading towards the zero-strain state (Fig. 15(a)), represented by the overall strain evolution $\overline{\boldsymbol{\varepsilon}}(t)$, with $\overline{\varepsilon}_{33} = \overline{\varepsilon}_{13} = \overline{\varepsilon}_{23} = 0$:

$$\begin{aligned} \overline{\boldsymbol{\varepsilon}}(0) = \begin{pmatrix} 0 & 0 \\ 0 & 0 \end{pmatrix} \rightarrow \overline{\boldsymbol{\varepsilon}}(T/4) = \begin{pmatrix} 0.04 & 0 \\ 0 & 0 \end{pmatrix} \rightarrow \overline{\boldsymbol{\varepsilon}}(T/2) = \begin{pmatrix} 0.04 & 0 \\ 0 & 0.04 \end{pmatrix} \\ \rightarrow \overline{\boldsymbol{\varepsilon}}(3T/4) = \begin{pmatrix} 0.04 & 0.04 \\ 0.04 & 0.04 \end{pmatrix} \rightarrow \overline{\boldsymbol{\varepsilon}}(T) = \begin{pmatrix} 0 & 0 \\ 0 & 0 \end{pmatrix} . \end{aligned} \tag{119}$$

- Non-proportional loading, consisting of different loading stages consisting of simultaneous bi- and uniaxial and shear deformation (Fig. 16(a)), represented by the overall strain evolution $\overline{\boldsymbol{\varepsilon}}(t)$, with $\overline{\varepsilon}_{33} = \overline{\varepsilon}_{13} = \overline{\varepsilon}_{23} = 0$:

$$\begin{aligned} \overline{\boldsymbol{\varepsilon}}(0) = \begin{pmatrix} 0 & 0 \\ 0 & 0 \end{pmatrix} \rightarrow \overline{\boldsymbol{\varepsilon}}(T/4) = \begin{pmatrix} 0.01 & 0.02 \\ 0.02 & -0.02 \end{pmatrix} \rightarrow \overline{\boldsymbol{\varepsilon}}(T/2) = \begin{pmatrix} 0.02 & 0 \\ 0 & -0.02 \end{pmatrix} \\ \rightarrow \overline{\boldsymbol{\varepsilon}}(3T/4) = \begin{pmatrix} 0.03 & -0.02 \\ -0.02 & -0.04 \end{pmatrix} \rightarrow \overline{\boldsymbol{\varepsilon}}(T) = \begin{pmatrix} 0.04 & 0 \\ 0 & -0.04 \end{pmatrix} . \end{aligned} \tag{120}$$

It is noted that the applied macroscopic deformation of up to 6 % goes far beyond the degree of deformation that the carbon fibers can sustain in reality. In the numerical applications in this work, where the fibers are assumed to deform purely elastic, this amount of deformation was applied to point out prediction differences of the nonlinear elasto-plastic behavior of the unit cell using the different models.

The predictions of the axial stress and the transverse strains in and out of the ply plane during the uniaxial tension test (Eq. (117)) and the shear stress response during the pure shear test (Eq. (118)) are compared in Fig. 10. The TFA allows a very high accuracy of the axial stress, while the HS approach leads to a slightly stiffer prediction (Fig. 10(b)). Considering the transverse strains in-plane (Fig. 10(c)) and out-of-plane (Fig. 10(d)), both TFA and HS methods deliver accurate results. The HS approach shows slight advantages over the TFA for the predictions of the in- and out-of-plane deformations. In particular, the HS type approach leads to less divergence from the DNS results of the out-of-plane deformation under the progression of the loading cycles. While both methods perform very well considering the in-plane and out-of-plane deformation during the first loading cycle, the HS approach delivers more accuracy during and at the end of the second loading cycle. Emphasized are the good predictions of the inelastic transverse deformation using the HS approach, in spite of the assumption of the constant Poisson ratio of the reference medium. Both methods perform very well and allow equivalently high accuracies of the shear stress evolution during the pure-shear test (Fig. 10(e)).

Besides the investigation of the homogenized macroscopic responses of the unit cell in Fig. 10, the strain evolutions and homogenized stress-strain responses of the yarns subdomains, following from the microstructural MFH, are evaluated during the first loading stage of the uniaxial tension test in $t = [0, 0.25]$. The reference results for the particular subdomains are provided by mesoscopic material points of the full-field FE solution, each located close

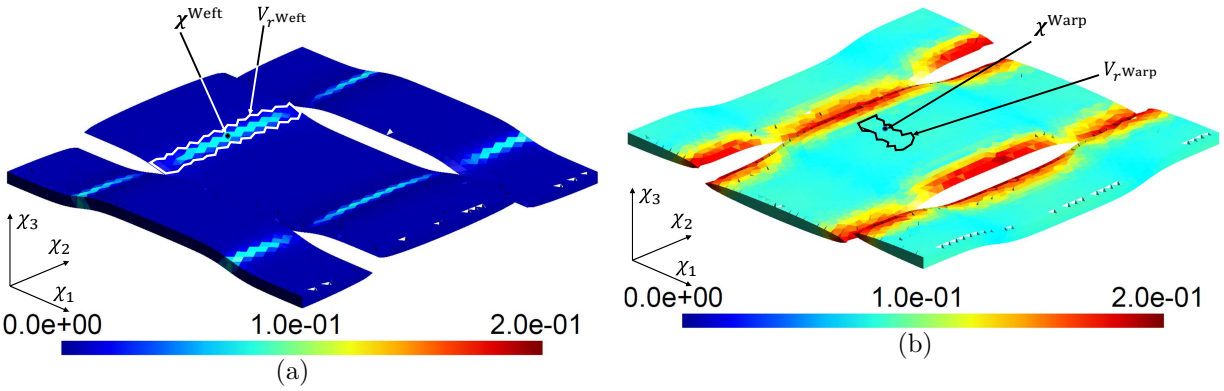

Figure 11: Locations of the selected subdomains $V_{r^{\text{Weft/Warp}}}$ and mesoscopic material points $\boldsymbol{\chi}^{\text{Weft/Warp}}$ in the (a) weft and (b) warp yarns for the investigation of the local yarn responses, computed by the MFH. Displayed are the equivalent plastic strain fields under the uniaxial tension test (Eq. (117)) in weft yarn direction at the end of the first loading stage $t = [0, 0.25], \bar{\varepsilon}_{11} = 0 \rightarrow 3\%$.

to the center of one of the considered subdomains. The two considered subdomains, $V_{r^{\text{Weft}}}$ and $V_{r^{\text{Warp}}}$, as well as the two associated mesoscopic reference material points, $\boldsymbol{\chi}^{\text{Weft}}$ and $\boldsymbol{\chi}^{\text{Warp}}$, are located in the inclined region of the weft yarn and in the planar region of the warp yarn, respectively. The specific locations of the considered mesoscopic material points and subdomains are indicated in Fig. 11. The mechanical behaviors of the subdomains, computed by the reduced models, and of the material points of the full-field solution, are displayed in Fig. 12. It is visible that the axial strain localization in the inclined region of the weft yarn, represented by the subdomain $V_{r^{\text{Weft}}}$, is slightly underestimated by both reduced models in comparison to the strain accumulated at the point $\boldsymbol{\chi}^{\text{Weft}}$ of the full-field solution. The stress-strain response of the same material point $\boldsymbol{\chi}^{\text{Weft}}$ of the full-field solution shows slightly nonlinear behavior towards the end of the loading stage. In comparison, the prediction of the subdomain $V_{r^{\text{Weft}}}$ by the HS type analysis is overstiff and appears elastic, while the prediction by the TFA shows overestimated inelastic effects and an underpredicted stress response of the same subdomain. The strain accumulation as well as the stress-strain response of the subdomain $V_{r^{\text{Warp}}}$, predicted by the HS type analysis, is in a high agreement with the behavior of the material point $\boldsymbol{\chi}^{\text{Warp}}$ of the full-field solution. Compared to that, the TFA leads to a clear overestimation of the strain accumulation in this region of the warp yarn. Furthermore, the axial stress decrease, observed in the full-field solution and reproduced by the HS type analysis, could not be modeled by the TFA.

In order to evaluate the validity of the selected offline deformation modes for more complex loading conditions, inelastic strain fields during and after the application of the two non-proportional deformation histories are inspected (Figs. 13 and 14). It can be recognized that the inelastic patterns in the yarns, even after the application of random loading paths, still correspond to the spatial division achieved by the subdomain decomposition based on the local yarn orientation and the plastic fields evolved during the selected static loading modes of the offline stage, displayed in Fig. 6.

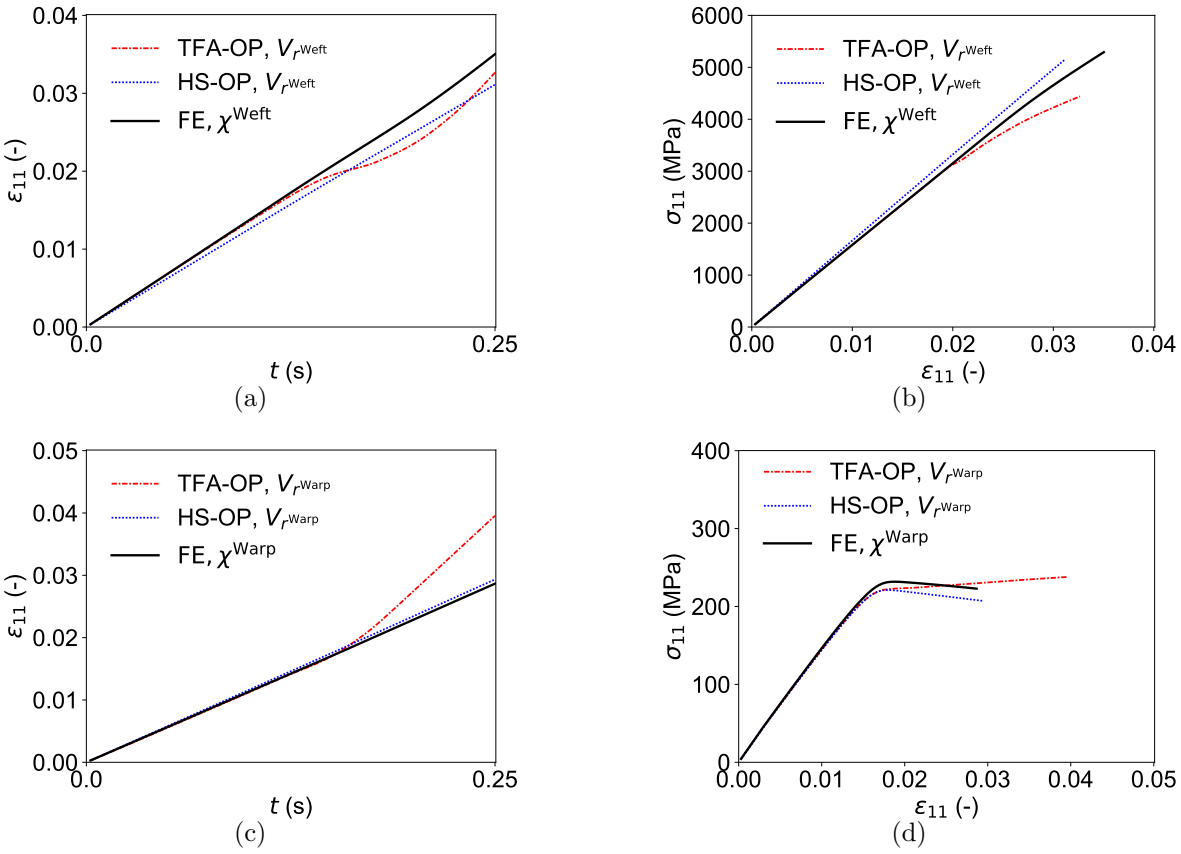

Figure 12: Local mesoscopic responses in the (a,b) weft and (c,d) warp yarns of the woven unit cell of the subdomains $V_{r^{\text{Weft/Warp}}}$ and mesoscopic material points $\boldsymbol{\chi}^{\text{Weft/Warp}}$ indicated in Fig. 11. Responses during the uniaxial tension test (Eq. (117)) in weft yarn direction during the first loading stage $t = [0, 0.25], \overline{\varepsilon}_{11} = 0 \rightarrow 3\%$: (a,c) strain evolutions and (b,d) stress-strain responses following from the microstructural MFH.

During the first non-proportional loading history given by Eq. (119), both the TFA and the HS approaches deliver high accuracies for the evolution of all stress components (Fig. 15). While the TFA perfectly covers both axial stresses during the complete loading history, the HS approach leads to very low stress over-estimations. The TFA captures the shear stress during the shear deformation loading stage very accurately, while the HS approach over-estimates the shear stress response. During the shear unloading stage, the TFA leads to an underestimation of the stress drop, while the HS approach allows a nearly perfectly matching final shear stress at the end of the applied loading. As recognized before, the TFA perfectly predicts both axial stress responses during the full non-proportional loading history given by Eq. (120) (Fig. 16). The HS approach leads to very light inaccuracies of the axial stresses. During the shear deformation, the TFA allows a perfect capture of the shear stress during the shear loading and unloading down to zero shear deformation. During the further shearing with negative sign however, the shear stress does not further drop as predicted by the FE and HS approach. Similarly, the shear stress increase predicted by the TFA during

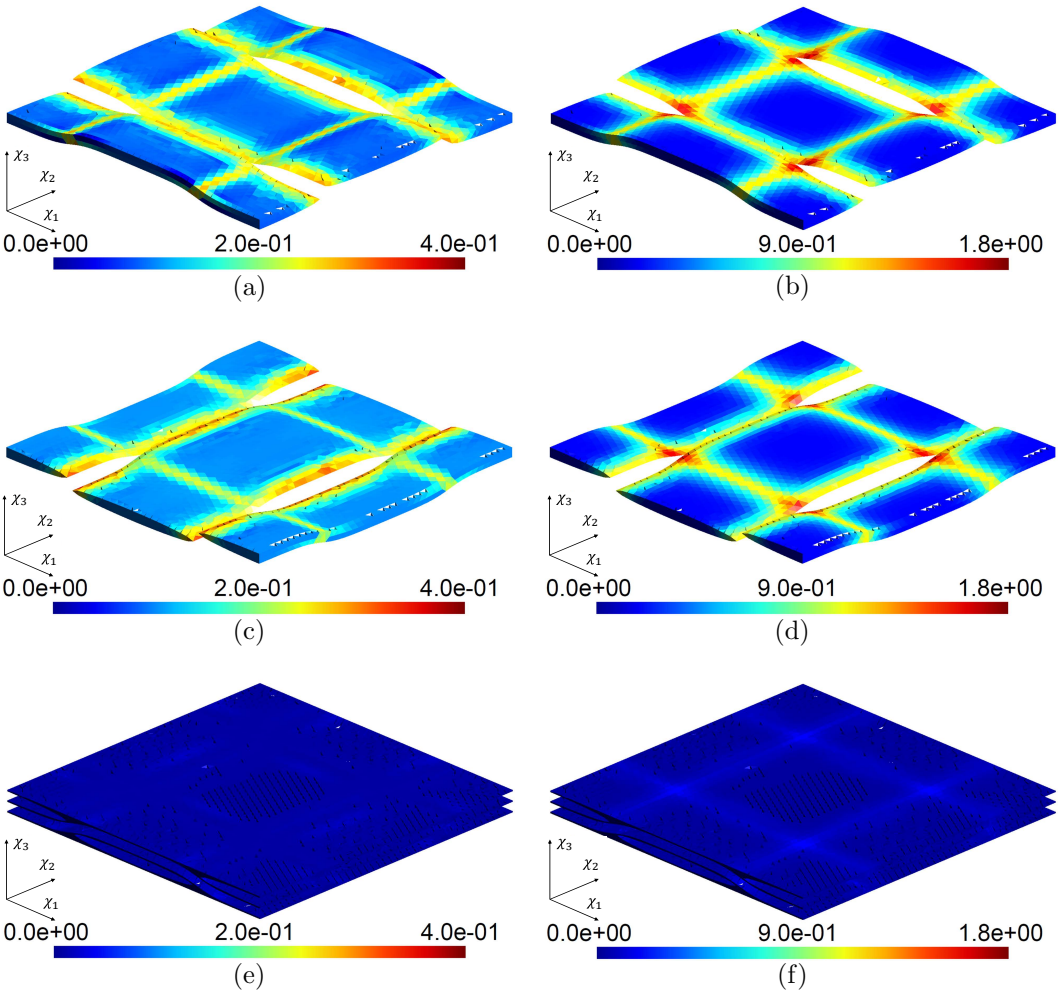

Figure 13: Equivalent plastic strain fields in the (a,b) weft yarn, (c,d) warp yarn and (e,f) matrix, (a,c,e) at $t = T/2$ and (b,d,f) at the end of the applied non-proportional loading history described by Eq. (119).

the following shear unloading towards a zero shear strain state is underestimated. Unlike the TFA, the HS approach allows very good agreements of the shear stress evolution during the full loading history.

Table 4: CPU time speed-ups for the non-proportional loading program in Eq. (120) using the TFA and HS algorithms.

method	TFA-O (K=20)	TFA-OP (K=68)	HS-O (K=20)	HS-OP (K=68)
speed-up	12e3	1.2e3	11e3	1.0e3

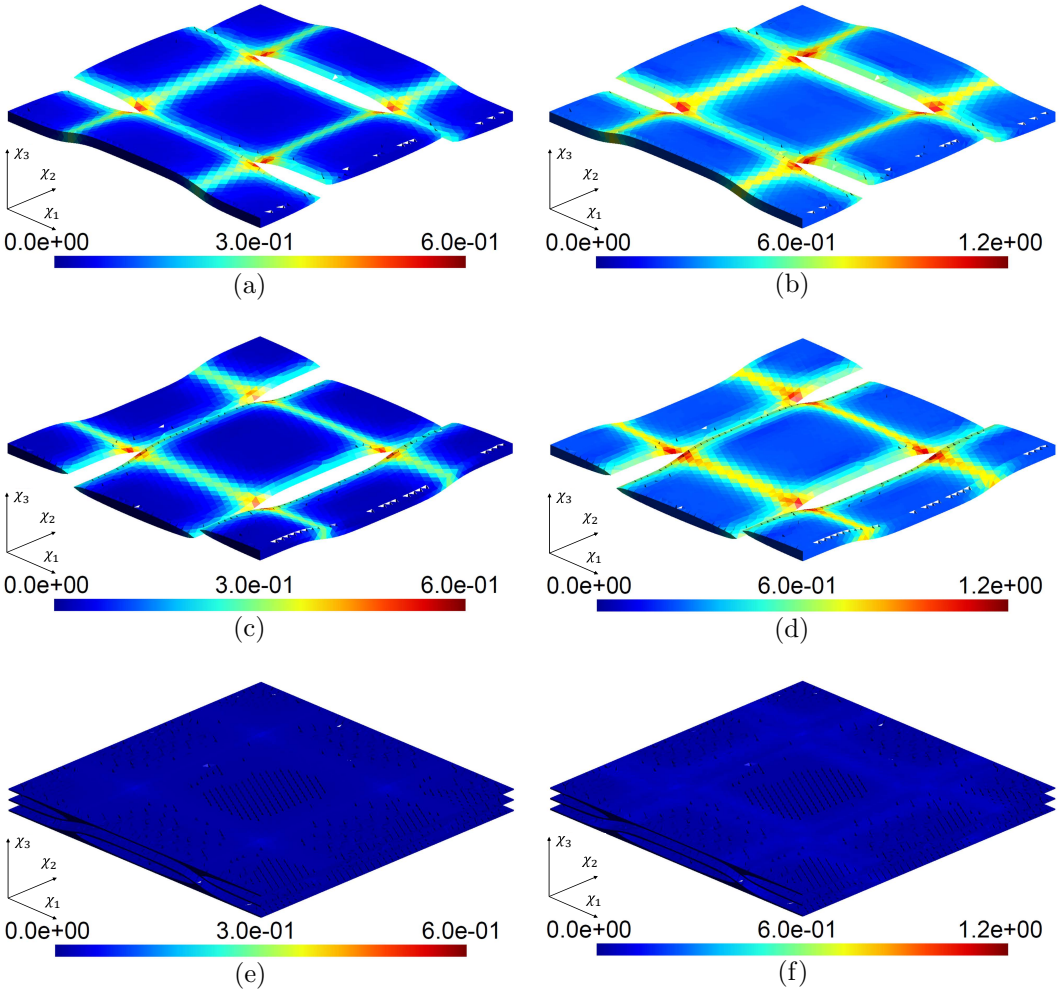

Figure 14: Equivalent plastic strain fields in the (a,b) weft yarn, (c,d) warp yarn and (e,f) matrix, (a,c,e) at $t = T/2$ and (b,d,f) at the end of the applied non-proportional loading history described by Eq. (120).

4.4. Discussion

It is shown that the selected static offline deformation modes for the woven unit cell allow an inelasticity-based spatial division that supports inelastic fields emerging under proportional and random loading conditions. The spatial decomposition based on the local yarn inclination alone provides, using the TFA, exact results for the elastic properties of the woven unit cell (Table 3), proving that the variation of the elastic properties are well respected. Moreover, the yarn orientation based decomposition allows to capture many of the inelastic localization zones in the woven structure. The subdomain refinement based on inelastic fields leads to only small improvements of the mechanical predictions. The yield points are captured more accurately, but the stiffness response during inelastic loading is generally captured equally well without the inelasticity-based subdomain refinement.

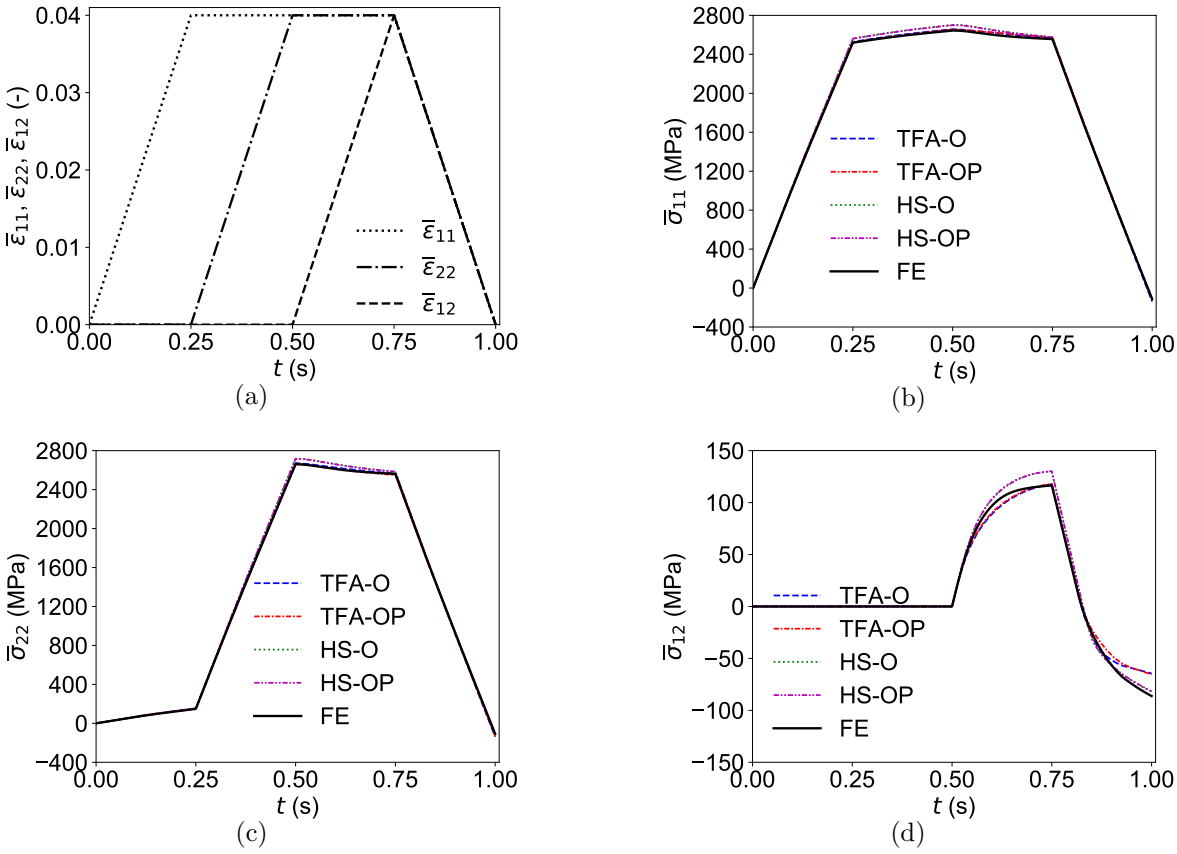

Figure 15: Applied loading history described by Eq. (119): evolution of the (a) applied strain path, normal stress responses in (b) χ_1-direction and (c) χ_2-direction, and (d) in-ply plane shear stress response.

Following the high accuracy of the representation of inelastic fields by the spatial division, the behaviors of the woven unit cell predicted by the ROM of inelastic loading show a very good agreement with the results achieved by DNS for all proportional and non-proportional inelastic loading histories. While the TFA provides slightly higher accuracies for axial stress responses, the HS approach allows better predictions for the transverse strains. Supported by well-covered inelastic localization zones during complex loading by the spatial decomposition, both approaches are well-capable to model the stress evolution during the applied non-proportional loading histories. Although both TFA and HS type analysis allow accurate predictions of the unit cell stress responses, it must be noted that the strain accumulations in the yarns, computed by the TFA, is not in accurate agreement with the DNS result. Observed during the uniaxial tension test, particularly the warp yarn (transversal to the loading direction) undergoes clearly too high deformation.

Comparing the computational efficiency of the ROM approach with respect to the DNS (Table 4), it becomes clear that the ROMs allow high time savings. While the use of 20 subdomains allow a computation that is 10 thousand times faster, the use of 68 subdomains still

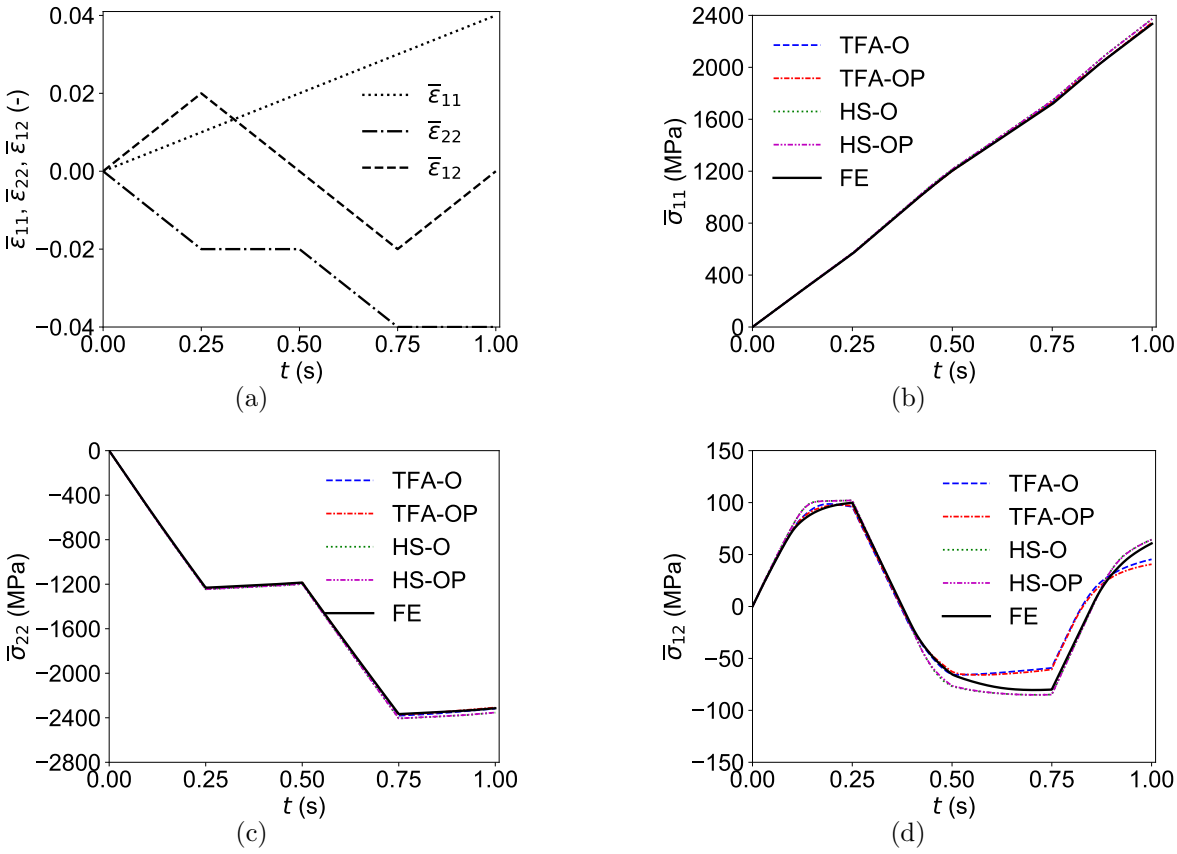

Figure 16: Applied loading history described by Eq. (120): evolution of the (a) applied strain path, normal stress responses in (b) χ_1-direction and (c) χ_2-direction, and (d) in-ply plane shear stress response.

allows an acceleration factor of 1 thousand. Additionally, the size of the numerical systems to be solved is much smaller using the ROMs, meaning that the required computational power is strongly reduced.

5. Conclusions

In this work, a two-step homogenization procedure for woven composites is employed, based on piecewise uniform ROM on the mesoscale and the MFH on the microscale. It allows for the efficient upscaling of the mechanical behavior from the microscale towards the mesoscale and finally the prediction of a macroscopic material point in the macroscale, represented by a woven unit cell.

Piecewise uniform field ROMs are used for the modeling of the macroscopic response of a woven composite unit cell. Each curved yarn is considered as one mesoscopic material phase, though the microstructure and the mechanical properties of the yarn materials are inhomogeneous as a consequence of the local yarn inclination. Therefore, a spatial decomposition into subdomains that takes into account the local orientation of the yarns is

essential for an accurate modeling of the elastic and inelastic responses. To this end, a spatial decomposition procedure is implemented, applicable for the mesoscopic model order reduction of three-scale materials that contain microstructures with heterogeneous stiffness fields due to non-uniform fiber/inclusion orientations. The predicted elastic responses of the woven unit cell are nearly exact, which proves that the orientation based clustering provides well-representative effective fiber orientations of the subdomains in the yarns.

Two ROM approaches were tested for the modeling of a woven composite unit cell. The TFA, typically leading to clearly overstiff inelastic predictions of composites with high volume fractions of stiff elastic inclusions in an elasto-plastic matrix phase, but allowing accurate results if both phases deform inelastically, and the HS approach, relying on a homogeneous and isotropic reference material. The elastic and inelastic responses of the woven composite, predicted by the ROMs, are in a good agreement with the responses modeled by DNS. The use of the MFH on the microscale means that a pre-determined yield criterion for the RVE as in Han et al. (2020), is not required, and enables mechanical predictions of the unit cell under arbitrary inelastic loading conditions. The high volume fraction of the stiff yarn material does not lead to inaccuracies using the TFA approach. As the TFA leads to typically overstiff responses for cases of stiff elastic fibers in an elasto-plastic matrix (Spilker et al., 2022, e.g.), it is concluded that the TFA benefits from the integration of the MFH for the yarn material, allowing the consideration of the yarn material as homogenized inelastic material phases. It is noted that, in particular during the uniaxial tension test, the elastic effective properties of the transverse yarn in the loading direction are in the same order of magnitude as the matrix material. To further test the TFA for cases where the yarns possess a higher elastic stiffness in the loading direction, and as glass fibers have isotropic elastic properties, the ROM results of a uniaxial tension test and a pure shearing test for the same woven composite unit cell with glass fiber reinforced yarns are reported in Appendix E. As for the case of carbon fiber reinforced yarns, very good homogenized predictions are accomplished when the carbon fibers are replaced by glass fibers. The HS approach, modified towards a tangent formulation in this work in order to remove inconsistencies of the homogenized response, is subject to only minor inaccuraries of the elastic response of the strongly anisotropic woven structure, although it relies on a virtual isotropic reference stiffness. It must be noted however, based on the results in Spilker (2022), that the validity of the HS type analysis can not be verified for general (strongly) anisotropic microstructures, where high errors of elastic and inelastic responses may occur. The accurate predictions for the elastic and inelastic responses of the woven unit cell under loading in the ply-plane can be explained by the orthotropic character of the unit cell with the same material properties of the warp and weft yarns, leading to same mechanical responses in both spatial directions in the ply-plane. Comparing the two implemented methods, it was observed that the TFA leads to more accurate homogenized predictions during elasticity and of the axial stress-strain responses, where the HS type analysis result is slightly overstiff. On the other hand, the HS type analysis allows better predictions of the strain accumulations in the yarns and of the homogenized transverse deformation.

In future works, the modeling capability for the mesoscale unit cell can be tested for damage occurring in the pure matrix and the yarns. To this end, the damage model needs

to be defined for the microscale and the mesoscale. The mesoscale unit cell is comprised by the pure matrix and the yarns subdomains. The damage of the yarns, consisting of fibers embedded in the matrix, would be modeled by the incremental-secant MFH on the microscale. A non-local damage model of the matrix was proposed by Wu et al. (2013b). A micromechanics-based extension for the incorporation of fiber breaking was developed by Wu et al. (2021b,c). The damage of the pure matrix of the unit cell would follow from a non-local damage law.

One main challenge for the ROMs originates from the high localization of damage. Compared to the onset of plastic yielding, which can, even with rather low numbers of subdomains, be well captured by the piecewise uniform approximations, the onset of damage occurs in highly localized zones. As shown by Liu et al. (2018), the predicted failure point is highly sensitive to the number of subdomains, and even elevated numbers of subdomains may not allow an accurate capture. In ductile materials, damage typically occurs in the zones of high plastic strain localizations. The inelasticity-based spatial decomposition (Spilker et al., 2022) may partially improve the capture of damage and failure, provided that the offline loading modes are well chosen. To alleviate the issue of the high dependence of the number of subdomains, Liu et al. (2018) proposed an regularization technique based on the consumed deformation energy until failure, for the calibration of damage parameters in dependence of the fineness of the spatial decomposition, enabling a good capture of the point of failure. The TFA and HS type analyses lead to similar predictions for the elasto-plastic response of the woven unit cell. However, the similar quality of the homogenized predictions may not apply for the case of damage. While the HS type analysis accurately represents the strain localization in the different unit cell phases, errors were found when using the TFA, implying the possibility of incorrect damage localizations and failure predictions. Furthermore, the reference medium of the HS type analysis represents the instantaneous response of the composite, and can therefore, as in the case of elasto-plasticity, as well adapt according to the response of the damaged composite with degraded elastic properties. Since the Green's interaction tensors are inversely proportional to the stiffness of the nonlinear reference medium (Eq. (13)), they can simply be scaled with respect to the reference stiffness, or solely the reference shear modulus as in Eq. (96), that represents the damaged composite. The concentration and interaction tensors of the TFA are functions of the composite medium with phases that have their initial elastic properties. The adaptation of these tensors would require to account for the changed elastic properties of the subdomains and of the composite medium, and is therefore more complex compared to the HS type analysis. Approaches for the damage modeling using the TFA were proposed by Kruch et al. (1996); Chaboche et al. (1998) and Chaboche et al. (2001).

The accurate predictions of the presented reduced three-scale bridging of the elasto-plastic woven composite unit cell are promising for the performance of unit cell based multiscale simulations of structural woven composites, using FE on the macroscale, with one macroscopic material point of the structure being represented by one woven unit cell. In the case of damage however, regularization should span the different macroscopic material points, introducing more complexity. Besides, for a realistic model on the structural scale, the integration of laminate layering imperfections and therefore the consideration of larger

RVEs instead of a unit cell may be required, particularly for the modeling of damage and failure of the structure.

Acknowledgement

The research has been funded by the Walloon Region under the agreement n^o.7911-VISCOS in the context of the 21st SKYWIN call.

Data availability

The raw/processed data required to reproduce these findings cannot be shared at this time as the data also forms part of an ongoing study.

Appendix A. Local yarn and fiber orientation in the woven composite

The yarn and fiber orientation at $\boldsymbol{\chi}$ is expressed as

$$\vec{v}(\boldsymbol{\chi}) = Q_2\big(\theta_2(\boldsymbol{\chi})\big) \cdot Q_1\big(\theta_1(\boldsymbol{\chi})\big) \cdot \vec{e}_3\,, \tag{A.1}$$

where $\vec{e}_3$ is the eigenvector in χ_3-axis direction of the unit cell reference system. The first Euler angle $\theta_1(\boldsymbol{\chi})$ represents a rotation with respect to the global coordinate system around the χ_3-axis, meaning

$$Q_1\big(\theta_1(\boldsymbol{\chi})\big) = \begin{bmatrix} \cos(\theta_1) & -\sin(\theta_1) & 0 \\ \sin(\theta_1) & \cos(\theta_1) & 0 \\ 0 & 0 & 1 \end{bmatrix}. \tag{A.2}$$

The second Euler angle represents a rotation of the once rotated coordinate system around the χ_1'-axis. Inside the rotated system, the second euler angle is therefore expressed as

$$Q_2\big(\theta_2(\boldsymbol{\chi})\big) = \begin{bmatrix} 1 & 0 & 0 \\ 0 & \cos(\theta_2) & -\sin(\theta_2) \\ 0 & \sin(\theta_2) & \cos(\theta_2) \end{bmatrix}. \tag{A.3}$$

The total local rotation matrix in Eq. (35) is given as

$$Q(\boldsymbol{\chi}) = Q_2\big(\theta_2(\boldsymbol{\chi})\big) \cdot Q_1\big(\theta_1(\boldsymbol{\chi})\big)\,. \tag{A.4}$$

Appendix B. MFH: Homogenized LCC operators

Using the Mori-Tanaka MFH formulation, the homogenized LCC stiffness can be computed from the corresponding phases LCC stiffnesses $\mathbb{C}_\omega^{\mathrm{LCC}}, \omega = \mathrm{I}, \mathrm{II}$ and the strain concentration tensor $\mathbb{B}_{\mathrm{II}}$ (Eq. (42)). The homogenized LCC operator reads

$$\mathbb{C}^{\mathrm{LCC}} = \big[\upsilon_{\mathrm{II}}\mathbb{C}_{\mathrm{II}}^{\mathrm{LCC}} : \mathbb{B}_{\mathrm{II}} + \upsilon_{\mathrm{I}}\mathbb{C}_{\mathrm{I}}^{\mathrm{LCC}}\big] : \big[\upsilon_{\mathrm{II}}\mathbb{B}_{\mathrm{II}} + \upsilon_{\mathrm{I}}\mathbb{I}\big]^{-1}, \tag{B.1}$$

so that, e.g., the homogenized elastic operator in Eqs. (49) and (58) and Fig. 3(a) reads

$$\mathbb{C}^{\mathrm{el}} = \big[\upsilon_{\mathrm{II}}\mathbb{C}_{\mathrm{II}}^{\mathrm{el}} : \mathbb{B}_{\mathrm{II}}^{\mathrm{el}} + \upsilon_{\mathrm{I}}\mathbb{C}_{\mathrm{I}}^{\mathrm{el}}\big] : \big[\upsilon_{\mathrm{II}}\mathbb{B}_{\mathrm{II}}^{\mathrm{el}} + \upsilon_{\mathrm{I}}\mathbb{I}\big]^{-1} \tag{B.2}$$

and the homogenized secant operator

$$\mathbb{C}^{\mathrm{sec}} = \big[\upsilon_{\mathrm{II}}\mathbb{C}_{\mathrm{II}}^{\mathrm{sec}} : \mathbb{B}_{\mathrm{II}}^{\mathrm{sec}} + \upsilon_{\mathrm{I}}\mathbb{C}_{\mathrm{I}}^{\mathrm{sec}}\big] : \big[\upsilon_{\mathrm{II}}\mathbb{B}_{\mathrm{II}}^{\mathrm{sec}} + \upsilon_{\mathrm{I}}\mathbb{I}\big]^{-1}. \tag{B.3}$$

Appendix C. MFH: Homogenized tangent

The homogenized algorithmic tangent stiffness is computed as

$$\mathbb{C}^{\mathrm{alg}} = \frac{\partial \boldsymbol{\sigma}}{\partial \boldsymbol{\varepsilon}} = \upsilon_{\mathrm{I}} \frac{\partial \boldsymbol{\sigma}_{\mathrm{I}}}{\partial \boldsymbol{\varepsilon}_{\mathrm{I}}} : \frac{\partial \boldsymbol{\varepsilon}_{\mathrm{I}}}{\partial \boldsymbol{\varepsilon}} + \upsilon_{\mathrm{II}} \frac{\partial \boldsymbol{\sigma}_{\mathrm{II}}}{\partial \boldsymbol{\varepsilon}_{\mathrm{II}}} : \frac{\partial \boldsymbol{\varepsilon}_{\mathrm{II}}}{\partial \boldsymbol{\varepsilon}} \,. \tag{C.1}$$

The algorithmic stiffnesses of the phases, $\partial \boldsymbol{\sigma}_{\omega} / \partial \boldsymbol{\varepsilon}_{\omega}$, follow from the computation of the stresses in Eqs. (55b) and (56), resulting in

$$\frac{\partial \boldsymbol{\sigma}_{\omega}}{\partial \boldsymbol{\varepsilon}_{\omega}} = \mathbb{C}^{\mathrm{sec}}_{\omega} + \frac{\partial \mathbb{C}^{\mathrm{sec}}_{\omega}}{\partial \boldsymbol{\varepsilon}_{\omega}} : \Delta \boldsymbol{\varepsilon}^{\mathrm{re}}_{\omega} \,. \tag{C.2}$$

Here, the inclusion phase behaves elastic, meaning that $\partial \boldsymbol{\sigma}_{\mathrm{II}} / \partial \boldsymbol{\varepsilon}_{\mathrm{II}} = \mathbb{C}^{\mathrm{el}}_{\mathrm{II}}$. The computation of the derivative of the matrix secant stiffness in Eq. (C.2), $\partial \mathbb{C}^{\mathrm{sec}}_{\mathrm{I}} / \partial \boldsymbol{\varepsilon}_{\mathrm{I}}$, is presented in Appendix D. The derivatives $\partial \boldsymbol{\varepsilon}_{\mathrm{I}} / \partial \boldsymbol{\varepsilon}$ and $\partial \boldsymbol{\varepsilon}_{\mathrm{II}} / \partial \boldsymbol{\varepsilon}$ follow from the MFH solution, presented in details by Wu et al. (2013a).

Appendix D. J_2-plasticity model: derivative of the incremental-secant operator by the strain

The derivative of the incremental secant operator following Eq. (68) with a pressure-independent plasticity, is given as

$$\frac{\partial \mathbb{C}^{\mathrm{sec}}_{\mathrm{I}}}{\partial \boldsymbol{\varepsilon}_{\mathrm{I}}} = 2\, \mathbb{I}^{\mathrm{dev}} \otimes \frac{\partial G^{\mathrm{sec}}_{\mathrm{I}}}{\partial \boldsymbol{\varepsilon}_{\mathrm{I}}} \,. \tag{D.1}$$

Consequently, the derivative of the incremental secant shear modulus

$$G^{\mathrm{sec}}_{\mathrm{I}} = \frac{\Delta \sigma^{\mathrm{re,eq}}_{\mathrm{I}}}{3\, \Delta \varepsilon^{\mathrm{re,eq}}_{\mathrm{I}}} \tag{D.2}$$

is to be computed. With

$$\frac{\partial \Delta \sigma^{\mathrm{re,eq}}_{\mathrm{I}}}{\partial \boldsymbol{\varepsilon}_{\mathrm{I}}} = \frac{3}{2} \frac{\mathrm{dev}(\Delta \boldsymbol{\sigma}^{\mathrm{re}}_{\mathrm{I}})}{\Delta \sigma^{\mathrm{re,eq}}_{\mathrm{I}}} : \mathbb{C}^{\mathrm{alg}}_{\mathrm{I}} = \frac{\mathrm{dev}(\Delta \boldsymbol{\sigma}^{\mathrm{re}}_{\mathrm{I}})}{2\, G^{\mathrm{sec}}_{\mathrm{I}} \Delta \varepsilon^{\mathrm{re,eq}}_{\mathrm{I}}} : \mathbb{C}^{\mathrm{alg}}_{\mathrm{I}} \tag{D.3}$$

and

$$\frac{\partial \Delta \varepsilon^{\mathrm{re,eq}}_{\mathrm{I}}}{\partial \boldsymbol{\varepsilon}_{\mathrm{I}}} = \frac{2}{3} \frac{\mathrm{dev}(\Delta \boldsymbol{\varepsilon}^{\mathrm{re}}_{\mathrm{I}})}{\Delta \varepsilon^{\mathrm{re,eq}}_{\mathrm{I}}} \,, \tag{D.4}$$

the derivative of the incremental secant shear modulus results in

$$\frac{\partial G^{\mathrm{sec}}_{\mathrm{I}}}{\partial \boldsymbol{\varepsilon}_{\mathrm{I}}} = \frac{1}{6\, G^{\mathrm{sec}}_{\mathrm{I}}\, (\Delta \varepsilon^{\mathrm{re,eq}}_{\mathrm{I}})^2} \mathrm{dev}(\Delta \boldsymbol{\sigma}^{\mathrm{re}}_{\mathrm{I}}) : \mathbb{C}^{\mathrm{alg}}_{\mathrm{I}} - \frac{2}{3} G^{\mathrm{sec}}_{\mathrm{I}} \frac{\mathrm{dev}(\Delta \boldsymbol{\varepsilon}^{\mathrm{re}}_{\mathrm{I}})}{(\Delta \varepsilon^{\mathrm{re,eq}}_{\mathrm{I}})^2} \,, \tag{D.5}$$

with the algorithmic tangent

$$\mathbb{C}^{\mathrm{alg}}_{\mathrm{I}} = \mathbb{C}^{\mathrm{el}}_{\mathrm{I}} - 2G^{\mathrm{el}}_{\mathrm{I}} \frac{\partial \Delta \boldsymbol{\varepsilon}^{\mathrm{p}}_{\mathrm{I}}}{\partial \boldsymbol{\varepsilon}_{\mathrm{I}}} = \mathbb{C}^{\mathrm{el}}_{\mathrm{I}} - \frac{(2G^{\mathrm{el}}_{\mathrm{I}})^2}{h_{\mathrm{I}}} \boldsymbol{N}_{\mathrm{I}} \otimes \boldsymbol{N}_{\mathrm{I}} - (2G^{\mathrm{el}}_{\mathrm{I}})^2 \frac{\Delta p_{\mathrm{I}}}{\Delta \sigma^{\mathrm{re,tr,eq}}_{\mathrm{I}}} \left(\frac{3}{2} \mathbb{I}^{\mathrm{dev}} - \boldsymbol{N}_{\mathrm{I}} \otimes \boldsymbol{N}_{\mathrm{I}} \right) , \tag{D.6}$$

where

$$h_{\mathrm{I}} = 3\, G^{\mathrm{el}}_{\mathrm{I}} + \frac{dR}{dp_{\mathrm{I}}} \,. \tag{D.7}$$

Appendix E. Mechanical predictions for a woven unit cell with glass fiber reinforced yarns

Table E.5: Material properties of the glass fiber reinforced woven composite unit cell.

Matrix (M10.1 epoxy)		Glass fiber	
Property	Value	Property	Value
Young's modulus E_{I} [GPa]	3.2	Young's modulus E_{II} [GPa]	75
Poisson ratio ν_{I} [-]	0.3	Poisson ratio ν_{II} [-]	0.2
Initial yield stress $\sigma_{\mathrm{I}}^{\mathrm{Y0}}$ [MPa]	30		
Hardening modulus H_{I} [MPa] (offline)	130		
Hardening exponent m_{I} [-]	300		

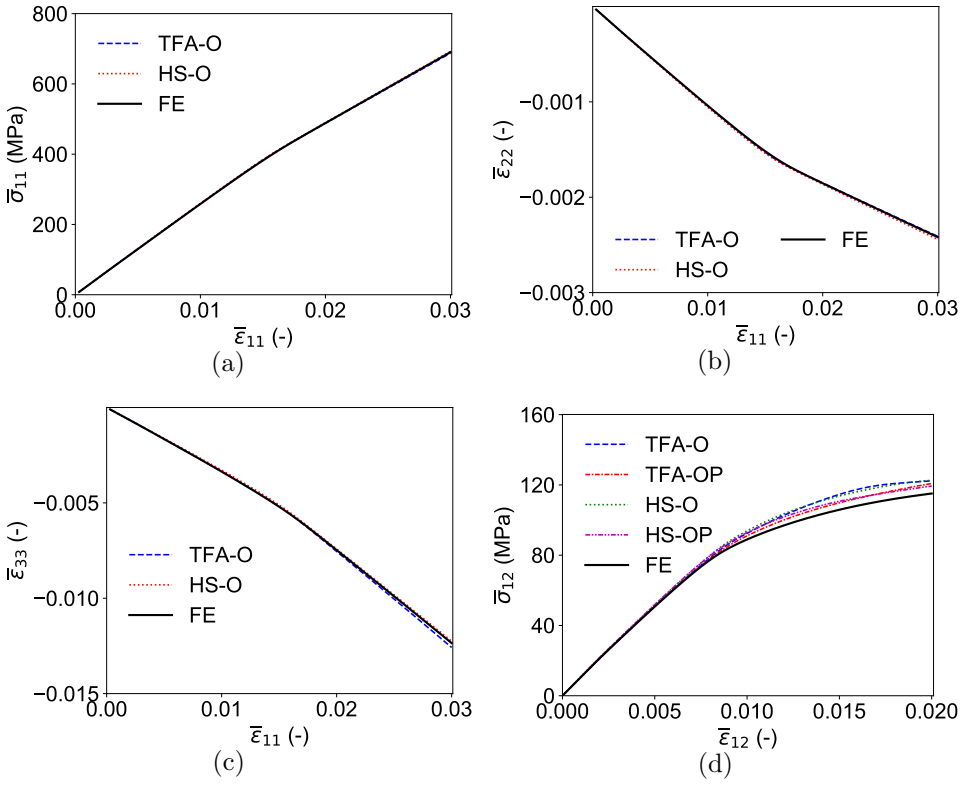

Figure E.17: Homogenized unit cell predictions during the first loading stages $t = [0, 0.25]$ of the (a-c) uniaxial tension test (Eq. (117)), $\overline{\varepsilon}_{11} = 0 \rightarrow 3\%$ and the (d) pure shear test (Eq. (118)), $\overline{\varepsilon}_{12} = 0 \rightarrow 2\%$: (a) axial stress-strain response, transverse strains (b) in- and (c) out-of-plane and (d) shear stress-strain response.

To further test the clustering based ROM methods, particularly the TFA, leading to overstiff results in cases of stiff elastic inclusions, another yarn material system was tested.

As the carbon fiber reinforced yarns have an effective transversal stiffness that is in the same order of magnitude as the matrix stiffness, it was investigated if the quality of the results is reduced when the stiffness contrast increases. For this matter, the carbon fibers were replaced by glass fibers, while the matrix material and the fiber volume fraction in the yarn material remain the same. Glass fibers have isotropic mechanical properties, leading to higher yarn stiffness in the yarns transverse direction. The material properties of both phases are reported in Table E.5. As visible in Fig. E.17, the results show high agreements of the predicted responses under the uniaxial tension as well as the pure shearing test by the ROM with the DNS.

References

Castrogiovanni, A., Marfia, S., Auricchio, F., Sacco, E., 2021. Tfa and hs based homogenization techniques for nonlinear composites. International Journal of Solids and Structures 225, 111050. URL: https://www.sciencedirect.com/science/article/pii/S0020768321001347, doi:https://doi.org/10.1016/j.ijsolstr.2021.111050.

Cavaliere, F., Reese, S., Wulfinghoff, S., 2020. Efficient two–scale simulations of engineering structures using the hashin–shtrikman type finite element method. Computational Mechanics 65, 159 – 175. URL: https://www.springerprofessional.de/en/efficient-two-scale-simulations-of-engineering-structures-using-/17118994, doi:10.1007/s00466-019-01758-4.

Chaboche, J., Kruch, S., Maire, J., Pottier, T., 2001. Towards a micromechanics based inelastic and damage modeling of composites. International Journal of Plasticity 17, 411–439. URL: https://www.sciencedirect.com/science/article/pii/S0749641900000565, doi:https://doi.org/10.1016/S0749-6419(00)00056-5.

Chaboche, J.L., Kruch, S., Pottier, T., 1998. Micromechanics versus macromechanics: a combined approach for metal matrix composite constitutive modelling. European Journal of Mechanics - A/Solids 17, 885–908. URL: https://www.sciencedirect.com/science/article/pii/S0997753898905009, doi:https://doi.org/10.1016/S0997-7538(98)90500-9.

Charalambakis, N., 2010. Homogenization Techniques and Micromechanics. A Survey and Perspectives. Applied Mechanics Reviews 63. URL: https://doi.org/10.1115/1.4001911, doi:10.1115/1.4001911, arXiv:https://asmedigitalcollection.asme.org/appliedmechanicsreviews/article-pdf/63/3/030803/5442740

de Souza Neto, E., Perić, D., Dutko, M., Owen, D., 1996. Design of simple low order finite elements for large strain analysis of nearly incompressible solids. International Journal of Solids and Structures 33, 3277–3296. URL: https://www.sciencedirect.com/science/article/pii/0020768395002596, doi:https://doi.org/10.1016/0020-7683(95)00259-6.

Doghri, I., Brassart, L., Adam, L., Gérard, J.S., 2011. A second-moment incremental formulation for the mean-field homogenization of elasto-plastic composites. International Journal of Plasticity 27, 352–371. URL: https://www.sciencedirect.com/science/article/pii/S0749641910000835, doi:10.1016/j.ijplas.2010.06.004.

Dvorak, G.J., 1990. On uniform fields in heterogeneous media. Proceedings of the Royal Society of London. Series A: Mathematical and Physical Sciences 431, 89–110. URL: https://royalsocietypublishing.org/doi/10.1098/rspa.1990.0120, doi:10.1098/rspa.1990.0120, arXiv:https://royalsocietypublishing.org/doi/pdf/10.1098/rspa.1990.0120.

Dvorak, G.J., 1992. On transformation strains and uniform fields in multiphase elastic media. Proceedings of the Royal Society of London. Series A: Mathematical and Physical Sciences 437, 291–310. URL: https://royalsocietypublishing.org/doi/10.1098/rspa.1992.0062, doi:10.1098/rspa.1992.0062, arXiv:https://royalsocietypublishing.org/doi/pdf/10.1098/rspa.1992.0062.

Eshelby, J.D., 1957. The determination of the elastic field of an ellipsoidal inclusion, and related problems. Proceedings of the Royal Society of London. Series A: Mathematical and Physical Sciences 241,

376–396. URL: https://royalsocietypublishing.org/doi/10.1098/rspa.1957.0133, doi:10.1098/rspa.1957.0133, arXiv:https://royalsocietypublishing.org/doi/pdf/10.1098/rspa.1957.0133.

Ferreira, B.P., Andrade Pires, F., Bessa, M., 2022. Adaptivity for clustering-based reduced-order modeling of localized history-dependent phenomena. Computer Methods in Applied Mechanics and Engineering 393, 114726. URL: https://www.sciencedirect.com/science/article/pii/S0045782522000895, doi:https://doi.org/10.1016/j.cma.2022.114726.

Feyel, F., 1999. Multiscale fe2 elastoviscoplastic analysis of composite structures. Computational Materials Science 16, 344–354. URL: https://www.sciencedirect.com/science/article/pii/S0927025699000774, doi:10.1016/S0927-0256(99)00077-4.

Fish, J., Shek, K., Pandheeradi, M., Shephard, M., 1997. Computational plasticity for composite structures based on mathematical homogenization: Theory and practice. Computer Methods in Applied Mechanics and Engineering 148, 53 – 73. doi:10.1016/S0045-7825(97)00030-3.

Fritzen, F., Leuschner, M., 2013. Reduced basis hybrid computational homogenization based on a mixed incremental formulation. Computer Methods in Applied Mechanics and Engineering 260, 143–154. URL: https://www.sciencedirect.com/science/article/pii/S0045782513000583, doi:10.1016/j.cma.2013.03.007.

Geers, M., Kouznetsova, V., Brekelmans, W., 2010. Multi-scale computational homogenization: Trends and challenges. Journal of Computational and Applied Mathematics 234, 2175–2182. URL: https://www.sciencedirect.com/science/article/pii/S0377042709005536, doi:https://doi.org/10.1016/j.cam.2009.08.077. fourth International Conference on Advanced COmputational Methods in ENgineering (ACOMEN 2008).

Geers, M.G.D., Kouznetsova, V.G., Matouš, K., Yvonnet, J., 2017. Homogenization Methods and Multiscale Modeling: Nonlinear Problems. Wiley. pp. 1–34. URL: https://onlinelibrary.wiley.com/doi/abs/10.1002/9781119176817.ecm2107, doi:10.1002/9781119176817.ecm2107, arXiv:https://onlinelibrary.wiley.com/doi/pdf/10.1002/9781119176817.ecm2107.

Han, X., Gao, J., Fleming, M., Xu, C., Xie, W., Meng, S., Liu, W.K., 2020. Efficient multiscale modeling for woven composites based on self-consistent clustering analysis. Computer Methods in Applied Mechanics and Engineering 364, 112929. URL: https://www.sciencedirect.com/science/article/pii/S0045782520301122, doi:https://doi.org/10.1016/j.cma.2020.112929.

Hashin, Z., Shtrikman, S., 1962. On some variational principles in anisotropic and nonhomogeneous elasticity. Journal of the Mechanics and Physics of Solids 10, 335–342. URL: https://www.sciencedirect.com/science/article/pii/0022509662900042, doi:10.1016/0022-5096(62)90004-2.

Hashin, Z., Shtrikman, S., 1963. A variational approach to the theory of the elastic behaviour of multiphase materials. Journal of the Mechanics and Physics of Solids 11, 127–140. URL: ttps://www.sciencedirect.com/science/article/pii/0022509663900607, doi:10.1016/0022-5096(63)90060-7.

Kanouté, P., Boso, D., Chaboche, J.e.a., 2009. Multiscale Methods for Composites: A Review. Archives of Computational Methods in Engineering 16, 31–75. URL: https://link.springer.com/article/10.1007%2Fs11831-008-9028-8#citeas, doi:10.1007/s11831-008-9028-8.

Kouznetsova, V., Brekelmans, W., Baaijens, F., 2001. An approach to micro-macro modeling of heterogeneous materials. Computational Mechanics 27, 37–48. URL: https://link.springer.com/article/10.1007/s004660000212, doi:10.1007/s004660000212.

Kröner, E., 1977. Bounds for effective elastic moduli of disordered materials. Journal of the Mechanics and Physics of Solids 25, 137–155. URL: https://www.sciencedirect.com/science/article/pii/0022509677900096, doi:https://doi.org/10.1016/0022-5096(77)90009-6.

Kröner, E., 1978. Self-consistent scheme and graded disorder in polycrystal elasticity. Journal of Physics F: Metal Physics 8, 2261–2267.

Kruch, S., Chaboche, J., Pottier, T., 1996. Two-scale viscoplastic and damage analysis of a metal matrix composite, in: Voyiadjis, G.Z., Allen, D.H. (Eds.), Damage and Interfacial Debonding in Composites. Elsevier. volume 44 of *Studies in Applied Mechanics*, pp. 45–56. URL: https://www.sciencedirect.com/science/article/pii/S0922538296800043, doi:https://doi.org/10.1016/S0922-5382(96)80004-3.

Lippmann, B.A., Schwinger, J., 1950. Variational principles for scattering processes. i. Phys. Rev. 79,

469–480. URL: https://link.aps.org/doi/10.1103/PhysRev.79.469, doi:10.1103/PhysRev.79.469.
Liu, Z., Bessa, M., Liu, W.K., 2016. Self-consistent clustering analysis: An efficient multi-scale scheme for inelastic heterogeneous materials. Computer Methods in Applied Mechanics and Engineering 306, 319 – 341. URL: http://www.sciencedirect.com/science/article/pii/S0045782516301499, doi:10.1016/j.cma.2016.04.004.
Liu, Z., Fleming, M., Liu, W.K., 2018. Microstructural material database for self-consistent clustering analysis of elastoplastic strain softening materials. Computer Methods in Applied Mechanics and Engineering 330, 547 – 577. URL: http://www.sciencedirect.com/science/article/pii/S0045782517307107, doi:10.1016/j.cma.2017.11.005.
Michel, J., Suquet, P., 2003. Nonuniform transformation field analysis. International Journal of Solids and Structures 40, 6937 – 6955. URL: http://www.sciencedirect.com/science/article/pii/S0020768303003469, doi:10.1016/S0020-7683(03)00346-9. special issue in Honor of George J. Dvorak.
Michel, J.C., Suquet, P., 2016. A model-reduction approach in micromechanics of materials preserving the variational structure of constitutive relations. Journal of the Mechanics and Physics of Solids 90, 254 – 285. URL: http://www.sciencedirect.com/science/article/pii/S0022509616300928, doi:10.1016/j.jmps.2016.02.005.
Moakher, M., Norris, A.N., 2006. The closest elastic tensor of arbitrary symmetry to an elasticity tensor of lower symmetry. Journal of Elasticity 85, 215–263. URL: http://dx.doi.org/10.1007/s10659-006-9082-0, doi:10.1007/s10659-006-9082-0.
Mori, T., Tanaka, K., 1973. Average stress in matrix and average elastic energy of materials with misfitting inclusions. Acta Metallurgica 21, 571–574. URL: https://www.sciencedirect.com/science/article/pii/0001616073900643, doi:10.1016/0001-6160(73)90064-3.
Moulinec, H., Suquet, P., 1994. A fast numerical method for computing the linear and nonlinear mechanical properties of composites. Comptes rendus de l'Académie des sciences. Série II. Mécanique, physique, chimie, astronomie. URL: https://hal.archives-ouvertes.fr/hal-03019226.
Moulinec, H., Suquet, P., 1998. A numerical method for computing the overall response of nonlinear composites with complex microstructure. Computer Methods in Applied Mechanics and Engineering 157, 69–94. URL: https://www.sciencedirect.com/science/article/pii/S0045782597002181, doi:10.1016/S0045-7825(97)00218-1.
Ponte Castañeda, P., 1991. The effective mechanical properties of nonlinear isotropic composites. Journal of the Mechanics and Physics of Solids 39, 45–71. URL: https://www.sciencedirect.com/science/article/pii/002250969190030R, doi:10.1016/0022-5096(91)90030-R.
Reuss, A., 1929. Berechnung der fließgrenze von mischkristallen auf grund der plastizitätsbedingung für einkristalle. Z. angew. Math. Mech. 9, 49–58.
Saeb, S., Steinmann, P., Javili, A., 2016. Aspects of computational homogenization at finite deformations: A unifying review from reuss' to voigt's bound. Applied Mechanics Reviews 68. URL: https://asmedigitalcollection.asme.org/appliedmechanicsreviews/article-abstract/68/5/050801/443653/Aspects-of-Computational-Homogenization-at-Finite?redirectedFrom=fulltext, doi:10.1115/1.4034024.
Spilker, K., 2022. Clustering Analysis for the Micromechanics-Based Reduced Homogenization in the Mechanics of Composite Materials. Ph.D. thesis. University of Liege. URL: https://orbi.uliege.be/handle/2268/296400.
Spilker, K., Nguyen, V.D., Adam, L., Wu, L., Noels, L., 2022. Piecewise-uniform homogenization of heterogeneous composites using a spatial decomposition based on inelastic micromechanics. Composite Structures 295, 115836. URL: https://www.sciencedirect.com/science/article/pii/S0263822322006018, doi:https://doi.org/10.1016/j.compstruct.2022.115836.
Talbot, D.R.S., Willis, J.R., 1985. Variational Principles for Inhomogeneous Non-linear Media. IMA Journal of Applied Mathematics 35, 39–54. URL: https://doi.org/10.1093/imamat/35.1.39, doi:10.1093/imamat/35.1.39, arXiv:https://academic.oup.com/imamat/article-pdf/35/1/39/2037184/35-1-39.pdf.
Voigt, W., 1889. Ueber die beziehung zwischen den beiden elasticitätsconstanten isotroper körper. Annalen

der Physik 274, 573–587.

Wu, L., Adam, L., Doghri, I., Noels, L., 2017. An incremental-secant mean-field homogenization method with second statistical moments for elasto-visco-plastic composite materials. Mechanics of Materials 114, 180–200. URL: https://www.sciencedirect.com/science/article/pii/S0167663617300698, doi:10.1016/j.mechmat.2017.08.006.

Wu, L., Adam, L., Noels, L., 2021a. Micro-mechanics and data-driven based reduced order models for multi-scale analyses of woven composites. Composite Structures 270, 114058. URL: https://www.sciencedirect.com/science/article/pii/S0263822321005183, doi:https://doi.org/10.1016/j.compstruct.2021.114058.

Wu, L., Maillard, E., Noels, L., 2021b. Tensile failure model of carbon fibre in unidirectionally reinforced epoxy composites with mean-field homogenisation. Composite Structures 273, 114270. URL: https://www.sciencedirect.com/science/article/pii/S0263822321007327, doi:https://doi.org/10.1016/j.compstruct.2021.114270.

Wu, L., Noels, L., Adam, L., Doghri, I., 2013a. A combined incremental-secant mean-field homogenization scheme with per-phase residual strains for elasto-plastic composites. International Journal of Plasticity 51, 80 – 102. URL: http://www.sciencedirect.com/science/article/pii/S0749641913001174, doi:10.1016/j.ijplas.2013.06.006.

Wu, L., Noels, L., Adam, L., Doghri, I., 2013b. An implicit-gradient-enhanced incremental-secant mean-field homogenization scheme for elasto-plastic composites with damage. International Journal of Solids and Structures 50, 3843–3860. URL: https://www.sciencedirect.com/science/article/pii/S0020768313003028, doi:https://doi.org/10.1016/j.ijsolstr.2013.07.022.

Wu, L., Zhang, T., Maillard, E., Adam, L., Martiny, P., Noels, L., 2021c. Per-phase spatial correlated damage models of ud fibre reinforced composites using mean-field homogenisation; applications to notched laminate failure and yarn failure of plain woven composites. Computers & Structures 257, 106650. URL: https://www.sciencedirect.com/science/article/pii/S0045794921001723, doi:https://doi.org/10.1016/j.compstruc.2021.106650.

Wulfinghoff, S., Cavaliere, F., Reese, S., 2018. Model order reduction of nonlinear homogenization problems using a hashin–shtrikman type finite element method. Computer Methods in Applied Mechanics and Engineering 330, 149 – 179. URL: http://www.sciencedirect.com/science/article/pii/S0045782517306904, doi:10.1016/j.cma.2017.10.019.

Yvonnet, J., 2019. Computational Homogenization of Heterogeneous Materials with Finite Elements. Solid Mechanics and Its Applications, Springer, Cham. URL: https://link.springer.com/book/10.1007/978-3-030-18383-7, doi:10.1007/978-3-030-18383-7.